REPORT DOCUMENTATION PAGE

2

Form Approved OMB NO. 0704-0188

1. REPORT DATE (DD-MM-YYYY)	2. REPORT TYPE	3. DATES COVERED (From - To)
31-07-2014	Ph.D. Dissertation	-

4. TITLE AND SUBTITLE
Optical forces near microfabricated devices

5a. CONTRACT NUMBER
W911NF-09-1-0473

5b. GRANT NUMBER

5c. PROGRAM ELEMENT NUMBER
611102

6. AUTHORS
Camilo A. Mejia Prada

5d. PROJECT NUMBER

5e. TASK NUMBER

5f. WORK UNIT NUMBER

7. PERFORMING ORGANIZATION NAMES AND ADDRESSES
University of Southern California
Contracts and Grants
3720 S. Flower Street
Los Angeles, CA 90089 -0701

8. PERFORMING ORGANIZATION REPORT NUMBER

9. SPONSORING/MONITORING AGENCY NAME(S) AND ADDRESS (ES)
U.S. Army Research Office
P.O. Box 12211
Research Triangle Park, NC 27709-2211

10. SPONSOR/MONITOR'S ACRONYM(S)
ARO

11. SPONSOR/MONITOR'S REPORT NUMBER(S)
56801-MS-PCS.13

12. DISTRIBUTION AVAILIBILITY STATEMENT
Approved for public release; distribution is unlimited.

13. SUPPLEMENTARY NOTES
The views, opinions and/or findings contained in this report are those of the author(s) and should not contrued as an official Department of the Army position, policy or decision, unless so designated by other documentation.

14. ABSTRACT
The PhD thesis theoretically proposes the idea of light-assisted, templated self assembly and describes its experimental demonstration. It is numerically demonstrated that trapped gold nanoparticles near a photonic-crystal microcavity form secondary traps for dielectric particles, allowing the formation of multi-particle clusters. Experiments on giant unilamellar vesicles in dual-beam optical traps are also described.

15. SUBJECT TERMS
optical forces, light-assisted self assembly, optical trapping, photonic crystals

16. SECURITY CLASSIFICATION OF:			17. LIMITATION OF ABSTRACT	15. NUMBER OF PAGES	19a. NAME OF RESPONSIBLE PERSON
a. REPORT	b. ABSTRACT	c. THIS PAGE			Michelle Povinelli
UU	UU	UU	UU		19b. TELEPHONE NUMBER 213-740-8682

Report Title

Optical forces near microfabricated devices

ABSTRACT

The PhD thesis theoretically proposes the idea of light-assisted, templated self assembly and describes its experimental demonstration. It is numerically demonstrated that trapped gold nanoparticles near a photonic-crystal microcavity form secondary traps for dielectric particles, allowing the formation of multi-particle clusters. Experiments on giant unilamellar vesicles in dual-beam optical traps are also described.

OPTICAL FORCES NEAR MICRO-FABRICATED DEVICES

by

Camilo Andrés Mejía Prada

A Dissertation Presented to the

FACULTY OF THE GRADUATE SCHOOL

UNIVERSITY OF SOUTHERN CALIFORNIA

In Partial Fulfillment of the

Requirements for the Degree

DOCTOR OF PHILOSOPHY

(PHYSICS)

August 2013

Acknowledgments

I would like to thank my advisor Dr. Michelle Povinelli for her support and guidance. Her expertise and knowledge lead us into great discussions concerning optical forces.

I thank Eric Jaquay and Dr. Luis Javier Martinez for developing the recipe for fabricating photonic crystal devices. They know that the path was difficult, but worth it.

I would also like to acknowledge Ningfeng Huang, Chenxi Lin, and Jing Ma for performing calculations and holding discussions relevant to this study.

I am grateful to Dr. Mehmet Solmaz for his mentoring in optical design and lab protocols. He put the experimental side of the laboratory to work. I also thank Roshni Biswas for performing relevant calculations and participating in discussions.

Finally, I thank Mia Ferrera Wiesenthal for rendering the schematic of LATS.

This work was funded by an Army Research Office Young Investigator Award under award No. 56801-MS-YIP and an Army Research Office PECASE Award under grant no. 56801-MS-PCS. Computation for work described in this dissertation was supported by the University of Southern California Center for High-Performance Computing and Communications (www.usc.edu/hpcc).

Contents

Acknowledgments ii

List of Figures v

Chapter 1 : Introduction 1
1.1 Forces . . . 4
1.1.1 Mechanical forces . . . 5
1.1.2 Van der Waals force . . . 6
1.1.3 Optical forces . . . 7
1.1.4 Thermal Gradient force . . . 12

Chapter 2 : Light Assisted template self-assembly 14
2.1 Design . . . 16
2.2 Optical force using guided modes . . . 16
2.3 Optical force maps and reconfiguration . . . 18
2.4 Inter-particle interaction . . . 20
2.5 Parametric dependency . . . 22
2.6 Experimental considerations . . . 23

Chapter 3 : Experimental demonstration of Light Assisted Template Self-assembly 25
3.1 Design . . . 26
3.2 Results . . . 27
3.3 Discussion . . . 30
3.4 Methods . . . 32
3.4.1 Fabrication . . . 32
3.4.2 Optical setup . . . 33
3.4.3 Stiffness analysis . . . 33
3.4.4 Force measurement . . . 34
3.4.5 Force and potential calculation . . . 35
3.5 Conclusions . . . 35

Chapter 4 : Optical trapping of Metal-dielectric cluster near a micro-cavity 38

4.1 Trapping of gold nano-particles 39
4.2 Cluster formation 44

Chapter 5 : GUV's Bending modulus measurement using Dual-beam optical trap 49
5.1 Stress profile 50
5.1.1 Surface stress using Ray Optics 51
5.1.2 Surface stress using the Maxwell Stress tensor 53
5.1.3 Comparison between RO and MST 54
5.2 Dual-beam optical trap setup 57
5.3 GUV fabrication 59
5.4 Trapping and stretching of GUVs 60
5.4.1 Calibration of optical forces 61
5.4.2 Temporal response to applied stress 62
5.5 Measurement of lipid bilayer bending modulus 63
5.6 POPC, POPC-col and DPPC bending modulus 68

List of Figures

2.1 Light-assisted templated self-assembly using a photonic crystal slab 15

2.2 (a) Normalized transmission of a silicon slab on a silica substrate for a height of $0.6a$ and hole radius of $0.2a$, (b) Force in the z direction for a sphere of radius $0.1a$ placed $0.25a$ above the slab surface. The sphere is positioned equidistant from the four closest holes. 17

2.3 Normalized intensity for normally incident x-polarized light for R1, R2, and R3, respectively at a height of (a-c) $0.25a$ above the surface of the slab and (d-f) $0.1a$ above the surface of the slab. White circles indicate hole positions. 18

2.4 (a-c) Force in the x-z plane at y = 0, (d-f) Force in the x-y plane at z = $0.25a$ for R1, R2, and R3, respectively. The red dots represent stable trapping points and the black circles indicate hole positions. 19

2.5 (a) Pattern for x-polarization, (b) Pattern for y-polarization. 20

2.6 (a) Schematic of the system (b) Transmission spectrum of photonic-crystal slab with and without particles above (c) $F_x c/\phi$ on particle 1 for 3 different positions of particle 2 (d) $F_y c/\phi$ on particle 1 for 3 different positions of particle 2. The legend indicates the position of particle 2 in (b), (c), and (d). 21

2.7 (a) Vertical force as a function of ϵ for a sphere with radius $0.15a$, (b) vertical force as a function of sphere radius for ϵ=3, (c) Vertical force for R1 as a function of ϵ for a sphere radius of $0.35a$. 23

2.8 (a) Vertical force as a function of ϵ for a sphere with radius $0.15a$, (b) vertical force as a function of sphere radius for ϵ=3, (c) Vertical force for R1 as a function of ϵ for a sphere radius of $0.35a$. 24

3.1 Schematic picture of templated, light-assisted self assembly. Incident light from below excites a guided-resonance mode of a photonic-crystal slab, giving rise to optical forces on nanoparticles in a solution. Under the influence of the forces, the nanoparticles self assemble into regular patterns. 26

3.2 (a) SEM image of photonic-crystal slab. The scale bar in the inset is 1 μm. (b) 3D FDTD simulation of the magnetic field (H_z) for a normally-incident, x-polarized plane wave. Circles represent the positions of holes; four unit cells are shown. (c) Measured transmission spectrum (log scale). 27

3.3 Light-assisted, templated self assembly of 520 nm diameter particles above a photonic-crystal slab. The square lattice of the slab is visible in the background, oriented at 45 with respect to the camera. (a-c) Sequential snapshots taken with the light beam on. (d) Snapshot taken after the beam is turned off. 28

3.4 Trap stiffness for incident, x-polarized light. (a) Particle positions (red dots) extracted from a 20-second video. Blue ellipses represent two standard deviations in position. (b) Histogram of stiffness values in the direction parallel to the polarization of the incident light. (c) Stiffness in the direction perpendicular to the incident polarization. 29

3.5 (a) Force map in one unit cell. The black circle represents the position of a hole, and the color bar represents the vertical optical force in dimensionless units of Fc/P, where c is the speed of light, and P is the incident optical power. A negative force indicates attraction toward the slab. The arrows represent the magnitude of the lateral optical force. The length of the white arrow at the bottom center of the figure corresponds to the maximum in-plane value of 1.6. (b) The potential through the center of the hole along the x-direction. The green dashed lines indicate the position of the hole. (c) The potential through the center of the hole along the y-direction. 31

4.1 (a) Schematic of defect cavity in a hexagonal lattice of holes with diameter d and thickness h, (b) Electric field distribution at the center of the slab at resonance, (c) Electric field distribution at z=130 nm above the slab at resonance, (d) Electric field distribution at z= 130 nm above the slab slightly off resonance. 41

4.2 Vertical force on gold nanoparticles of different sizes and a dielectric particle with r = 80 nm and ϵ = 1.59. 42

4.3 Gradient (a), and scattering and absorption forces (b) on a gold particle with r = 80nm using the dipole approximation. 43

4.4 (a) Vertical force as a function of frequency for several different vertical positions. Normalized force in the (b) horizontal and (c) vertical directions as a function of position in the x-y plane for a gold particle with r = 80nm. 44

4.5 Electric field intensity in the midplane (a) and on a vertical cut (b) of a trapped gold particle with r = 80 nm. Horizontal (c) and vertical (d) optical forces as a function of position for a dielectric particle with r = 80 nm in the presence of a trapped gold particle (yellow circle). (e) Horizontal optical force as a function of position for a dielectric particle near trapped gold (yellow) and dielectric (blue) particles. The arrows next to the graph represent Fc / flux = 0.002. 45

4.6 Force on gold particle due to dielectric particle. 47

5.1 Dual-beam optical trap 50

5.2 (a) Optical stress for multiple reflections on a spheroid with volume equal to a 5 μm sphere and e = 0.4 (n_1 = 1.335, n_2 = 1.38, w = 11 μm). RI of Red Blood Cells is close to the value chosen in this case. (b) Total optical surface stress in the equatorial plane for single beam, and (c) total optical surface stress for dual beam. 52

5.3 Circularly polarized electric field intensity and corresponding stress profile in the equatorial plane for (a) Single Beam (b) Dual beam. 54

5.4 Comparison of stress profile arising from single beam in the equatorial plane obtained from ray optics and MST for varying eccentricities (b) single beam electric field intensity profile corresponding to $e = 0.0$ and $e = 0.9$ (c) Dual beam. 55

5.5 Comparison of MST and RO for spheroids with e = 0.4 (a) refractive index variation and (b) size variation. 57

5.6 (a) Schematic of the stretching of a GUV using DBOT, (b) Optical setup that incorporates a silicon chip for fiber-to-capillary alignment and microfluidic adapters to couple the flow channel. 58

5.7 (a) POPC-GUV optically trap at low power, (b) POPC-GUV optically trap at high power, (c) A plot of the contours fitted to both stretching powers (blue = low power / low tension, green = high power / high tension). The scale bar is 10 μm. 61

5.8 The drag forces in no-slip and perfect-slip cases are plotted against the calculated optical forces (solid lines) from one beam for two power levels, 50mW and 100mW. 50 μm corresponds to the center of the channel. 62

5.9 (a) The optical power (blue line; right axis) is suddenly increased from 100 mW to 500 mW. The major axis strain is shown by the red dots (left axis). (b) Micrograph of deforming GUV. The scale bar is 10 μm. 63

5.10 Measurement of the bending modulus of a pure POPC GUV. Time axis is common to plots a-c, dotted guide lines show time points at which laser power is increased. (a) Laser power as a function of time. (b) 2D contour plot showing the radius as a function of angle in the image plane as a function of time. (c) Percentage area strain as a function of time. (d) Average stress on the GUV as a function of eccentricity and base radius. (e) Average percentage area strain for each laser power plotted versus the scaled lateral tension. κ is the fitted value of the bending modulus. 64

5.11 Apparent area strain versus ln(tension) plots for POPC and DPPC GUVs with 20% cholesterol. The POPC lipid membrane is more flexible than DPPC lipid membrane. The error bars represent one standard deviation of area strain and lateral tension. The errors in bending modulus values are calculated from the standard errors of the slope using linear regression analysis. 69

5.12 Histograms of the bending modulus distributions of and DPPC-Chol, POPC-Chol, and pure POPC lipid GUVs. 70

5.13 Laser power ramp-up and ramp-down experiments on two different GUVs, (a) POPC and (b) DPPC-20%Chol. 73

Chapter 1

Introduction

In recent years, new complex structures have been fabricated on the nano-scale which exhibit novel optical properties. An example of such devices include Photonic crystals (PhC). A PhC is a periodic refractive index perturbation in a high-index material. These man-made structures can forbid light propagation within certain frequency ranges and demonstrate novel dispersion characteristics (1).

In order to fabricate such complex structures, new techniques have been developed; one particular method involves particle self-assembly. In the self-assembly method (2) particles are deposited upon a substrate and organize themselves in a form determined by their inter-particle interactions. A fundamental constraint, however, in the self-assembly method is that only energetically favorable structures are formed. Templated self-assembly methods have been introduced (3; 4) to expand the range of structures that can be fabricated using self-assembly. In this method, particle assembly occurs on a template. The geometry of the template guides particle arrangement, allowing the formation of diverse crystal structures. A fundamental problem with this method is that the final structure is determined strongly by the geometry of the template. Consequently, the formation of structures that possess different size particles and a wide range of material, is not well controlled.

On the other hand, since the discovery of optical tweezers (5; 6), optical forces near micro-photonic devices have been studied extensively. While standard optical tweezers

use a focused laser beam to trap and manipulate particles, structured light fields allow even greater control. Large optical forces have been achieved by using the strong electromagnetic fields near nano-apertures (7), gratings (8), photonic-crystal micro-cavities (9; 10), slot waveguides (11) and plasmonic structures (12; 13). Applications of such particle manipulation have been found from the physical sciences to biology (14; 15). However, much of this work has only considered single-particle traps.

In this dissertation, I study optical forces near micro-fabricated devices for multi-particle manipulation. I consider particles of different sizes and compositions. In particular, I focus my study on both dielectric and gold particles as well as Giant Unilamellar Vesicles (GUVs).

First, I consider optical forces near a PhC and establish the feasibility of a technique which we term *Light-Assisted Templated Self-assembly* (LATS). In contrast to previous work on Fabry-Perot enhancement of trapping forces above a flat substrate (16), I exploit the guided resonance modes of a PhC (17) to provide resonant enhancement of optical forces. The guided mode forms spatially distinct trapping patterns at different polarizations and wavelengths. I consider the possibility of assembling multi-particle patterns. Specially, I show how optical forces near a photonic crystal slab can be used to assist templated self-assembly and permit different particle pattern formation. Thus, a PhC will serve as an optically reconfigurable template for multi-particle trapping.

Furthermore, in contrast to localized mode trapping techniques (which is necessarily limited to a smaller area, and thus, fewer trap sites) the use of an extended mode has obvious advantages. The fact that every trap operates simultaneously in a small area eliminates the need for a spatial light modulator or beam scanning of the sample. This

is a unique feature of our extended-mode trapping system.

Combining the optical field created in our system with a microfluidic flowalso provides the potential for sorting particles via the creation of lock-in states (18). Additionally, changing the shape of the hole within each unit cell, an asymmetric potential could be created which could operate as a ratchet (19). We anticipate that our system could be applied in self-assembly experiments and also to build clusters in a reversible way; the later would enable the creation of reconfigurable, optical matter (20). Our LATS system is able to assemble structures with arbitrary symmetries which are ordinarily unavailable for assembly due to energy constraints. We demonstrate this unique ability both theoretically and experientally. In addition, our structure could be fabricated upon an active material, thereby merging the source and trap. With proper electrical excitation, such structures could easily be adopted for various applications. Finally, although previous work has examined light forces between different layers of particles in colloidal PhC (21; 22), forces on colloidal layers above a micro-fabricated template were not considered. I used full-vectorial electromagnetic simulations of Maxwell's equations in time domain to calculate optical forces on dielectric particles of ~ 500 nm.

In Chapter 3, I present the experimental demonstration of LATS. I explain all relevant setup and fabrication methods. Next, I use a particle tracking software to record the position of a 520 nm polystyrene particle while trapped in a square lattice PhC. In addition, I numerically calculate the optical force at the center of the trapping pattern and the corresponding optical stiffness of the PhC trap.

In the following chapter, I calculate the optical force near a PhC micro-cavity for gold and dielectric particles $\sim$ 50 nm in diameter in diameter. Next, I use the electromagnetic field re-distribution around a trapped gold nano-particle to direct a metal-dielectric cluster formation.

In the final chapter, I explore optical forces near a Dual Beam Optical Trap (DBOT) and measure the bending modulus of a GUV $\sim$ 10 μm. First, I present a method to extract the bending modulus of the membrane from the area strain data. This method incorporates three-dimensional ray-tracing to calculate the applied stress in the DBOT within the Ray Optics approximation. I compare the optical force calculated using the Ray Optics approximation and Maxwell Stress Tensor method the ensure the approximation's accuracy. Next, we apply this method to 3 populations of GUVs to extract the bending modulus of membranes comprised of saturated and monounsaturated lipids in both gel and liquid phases. We find that bending modulus values depend on lipid phase and are normally distributed for the three populations we tested. Our results also indicate that the addition of cholesterol to POPC membranes does not alter the respective bending modulus. Moreover, the values we obtain for bending moduli agree well with those found in literature. This technique is a promising route to obtaining statistically relevant bending moduli data for lipid membranes with controlled compositions.

1.1 Forces

For a particle in water, we can consider the interplay of various forces: gravitational, buoyant, brownian, electrostatic and those forces that develop from the interaction

between an external electromagnetic field and a particle. I'll refer to the last one as an optical force.

In general, the dynamics of the particle is governed by the following equation:

$$m\ddot{\vec{x}} = -\gamma\dot{\vec{x}} + \vec{F}_{fluid} + \vec{F}_{optical} + \vec{\chi}(t) \tag{1.1}$$

where γ is the friction coefficient, and $\chi_i(t)$ are mutually uncorrelated white noises that obey the fluctuation-dissipation relation $\langle\chi_i(t)|\chi_j(t)\rangle = 2k_BT\gamma\delta_{ij}\delta(t-t')$.

In this chapter, I describe the origin and order of magnitude for these forces acting upon a 1 μm polystyrene particle.

1.1.1 Mechanical forces

In the particular case of a polystyrene particle in water ($\rho_{water} = 1g/cm^3, \eta_{water} = 1.3\times10^{-4}cm^2/s, \rho_{poly} = 2.5g/cm^3$), the gravitational force is on the order of 1×10^{-2} pN while the buoyancy force is $\sim 0.6\times10^{-2}$ pN. Thus, the particle feels a net gravitational force on the order of $\sim 1\times10^{-3}$ pN.

Using the diffusion coefficient $D = k_BT/6\pi r\eta = 0.5\mu m^2/s$ as well as the drag coefficient $\gamma = 6\pi r\rho\eta$, the average Brownian force can be shown to be $\sim 1\times10^{-4}$ pN.

For this system the Reynolds number is $\sim 1\times10^{-7}$. At a low Reynolds number, the inertia plays no role in the particle dynamics whatsoever. That means, what the particle is doing at any given moment is entirely determined by the forces that are

exerted on particle at that moment, and by nothing in the past. Thus, Eq. (1.1) reduces to

$$\gamma\dot{\vec{x}} = \vec{F}_{fluid} + \vec{F}_{optical} + \vec{\chi}(t) \tag{1.2}$$

1.1.2 Van der Waals force

The Van der waals force arises from electron cloud fluctuations surrounding the nucleus of an electrically neutral atom. This force is a short range force and, in generally, is attractive.

For macroscopic bodies with known volumes and numbers of atoms (molecules per unit volume), the total van der Waals force is often computed based on the microscopic theory as the sum over all interacting pairs. It is necessary to integrate over the total volume of the object, which makes the calculation dependent on the object's shape.

The van der Waals force between two spheres of constant radii R_1 and R_2 is then a function of separation r

$$F_{VW} = -\frac{AR_1R_2}{6r^2(R_1 + R_2)} \tag{1.3}$$

where A is a constant that depends on both materials. For two 500 nm polystyrene particles in water, $A = 0.22 \times 10^{-20} J$ and $F = 1 \times 10^{-3}$ pN at 300 nm of separation.

In the case of a sphere near a surface, the van der Waals force is

$$F_{VW} = \frac{AR}{6r^2} \tag{1.4}$$

For a 500 nm particle floating in water 100 nm from a silicon surface $F = 1 \times 10^{-3}$ pN.

1.1.3 Optical forces

Optical forces arise whenever an electromagnetic wave propagates in a medium. It can be understood as a change in momentum of the propagating light due to a change in refractive index; it is a force felt by the induces dipoles in the medium due to the presence of an electromagnetic field.

Maxwell stress tensor method

For a small volume V the induced charge ρ will experience a mechanical force given by the Lorent's relation (23):

$$\vec{F} = \int_V (\rho\vec{E} + \vec{J} \times \vec{B})dV \tag{1.5}$$

Expressing the charge, current and magnetic field in terms of the total electric field $\vec{E}$ we can obtain

$$\vec{F} = \oint_{\delta S} \vec{T_\alpha} \cdot d\vec{a} - \frac{d\vec{S}}{dt} \tag{1.6}$$

where δS is the surface enclosing the volume V, $\vec{S}$ is the Poynting vector and $T_{\alpha\beta}$ is the Maxwell stress tensor defined as

$$T_{\alpha\beta} = D_\alpha E_\beta - \frac{1}{2}\delta_{\alpha\beta}(\vec{D} \cdot \vec{E}) + H_\alpha B_\beta - \frac{1}{2}\delta_{\alpha\beta}(\vec{H} \cdot \vec{B}) \tag{1.7}$$

In general, there are two natural approximations often employed in such calculations: particles much smaller than the wavelength (dipole approximation) or much larger (ray optics).

Optical force using dipole approximation

Let us write Eq. (1.6) in the volume form (24; 25)

$$\langle \vec{F} \rangle = \oint_{\delta S} \langle \vec{T}_\alpha \rangle \cdot d\vec{a} = \int d^3\vec{r}\, \nabla \langle T(r) \rangle \tag{1.8}$$

For a small particle, the total field inside the particle can be expressed in terms of the external field $\vec{E}_0(\vec{r})$ as

$$E(r) = E_0(r) + \alpha G(r - r_0) E_0(r) \tag{1.9}$$

where G is the Green function,

$$G_{ij}(r) = (k_0^2 \delta_{ij} + \partial_i \partial_j) \frac{e^{ik_0 r}}{4\pi\epsilon_0 r} \tag{1.10}$$

and α is the polarizability

$$\alpha = \frac{\alpha_0}{1 - i\alpha_0 k_0^3/(6\pi\epsilon_0)}, \;\; \alpha_0 = 4\pi\epsilon_0 a^3 \frac{\epsilon - 1}{\epsilon + 1}. \tag{1.11}$$

The time average force, expresed in terms of the external electric field and the induced dipole moment is (26)

$$\langle \vec{F} \rangle = \frac{1}{2} Re \left[\sum_i p_i \nabla E_{0i}^* \right] = \frac{1}{2} Re \left[\sum_i \alpha E_{0i} \nabla E_{0i}^* \right] \tag{1.12}$$

using Faraday's law $\nabla \times E = i\omega\mu_0 H$ and the relation $\sum_i E_i \nabla E_i^* = (E \cdot \nabla)E^* + E \times (\nabla \times E)$, the dipolar force $\langle \vec{F} \rangle$ can be expand as the sum of the gradient force, radiation pressure and spin density of the light field as

$$\langle \vec{F} \rangle = \frac{1}{2} Re\left[\alpha E_0 \cdot \nabla E_0\right] + \sigma_{scat}\left[\frac{1}{c}\langle \vec{S} \rangle\right] + \sigma_{scat}[c\nabla \times \langle \vec{L_S} \rangle] \tag{1.13}$$

where $\sigma_{scat} \equiv k_0 Im(\alpha)/\epsilon_0$ is the scattering cross section and $\langle \vec{L_S} \rangle = \frac{\epsilon_0}{4i\omega}(\vec{E_0} \times \vec{E_0^*})$ is the time averaged spin density.

The first term is the gradient force, the second term is the radiation pressure (proportional to the Poynting vector $\langle \vec{S} \rangle$), and the last term is a curl force associated to the nonuniform distribution of the spin density of the light field.

Optical binding

The dipole approximation done in Eq. (1.13) is valid for a single particle in an external field. For multiple particles, the total electric field is the superposition of the incident electric field and the field emitted by the induced dipoles.

Let us consider two dielectric particles with induced dipole moments $\vec{p}(r_A)$ and $\vec{p}(r_B)$ in an electric field $\vec{E}$ such that, $p_i(r_{A|B}) = \alpha_{ij}^{A|B} E_j(r_{A|B})$. In terms of the incident field $\vec{E_0}$, the total field can be rewritten as (27):

$$\begin{aligned} E_i(r_A) &= E_{0i}(r_A) + G_{ij}(r_A, r_B)\alpha_{jk}^B E_k(r_B) \\ E_i(r_B) &= E_{0i}(r_B) + G_{ij}(r_B, r_A)\alpha_{jk}^A E_k(r_A). \end{aligned} \tag{1.14}$$

The solution for particle B of this equation is $E_i(r_B) = K_{ij}E_{0j}(r_B) + K_{ij}G_{jk}\alpha_{km}^A E_{0m}(r_A)$, where K_{ij} is the inverse tensor, $[I - G(r_B, r_A)\alpha^A G(r_A, r_B)\alpha^B]^{-1}$.

For small particles we can approximate $K_{ij} \cong \delta_{ij}$, thus, Eq. (1.12) for particle B can be written as

$$\begin{aligned} F_\gamma(r_B) = \quad & \frac{1}{2} Re[\alpha_{ij}^{B*} E_{0j}^*(r_B) \partial_\gamma^B E_{0i}(r_B) \\ & + \alpha_{ij}^{B*} G_{jk}^* \alpha_{km}^{A*} E_{0m}^*(r_A) \partial_\gamma^B E_{0i}(r_B) \\ & + \alpha_{ij}^{B*} E_{0j}^*(r_B) \partial_\gamma^B G_{iq} \alpha_{qn}^{A} E_{0n}(r_A)]. \end{aligned} \tag{1.15}$$

The first term is the classical formula for the optical force which is determined solely by the spatial distribution of the incident field. This force is usually further divided into both a gradient force and scattering force. The second term is the interaction between the incident field and the induced dipole from the scattered field. The third term corresponds to the force acting upon the induced dipole from the scattered field by the incident field.

In general, by using the Maxwell stress tensor method we incorporate the effect of optical binding.

Optical force in the ray optics approximation

For particles much larger than the wavelength of the incident light, we can use the Ray Optics approximation (RO). Under this assumption, rays undergo a change in momentum after a reflection on a surface. This change in momentum induces an optical force on the object.

Let us consider a ray propagating along the incident direction $\hat{i}_0$. This ray carries a momentum of $\vec{p} = (n_1/c) P \hat{i_0}$, where n_1 is the refractive index of the medium, P is the optical power and c is the velocity of light in vacuum. Following a reflection, the force

acting upon a surface can be calculated as the difference in momentum carried by the incident ray compared to that carried by both the reflected and transmitted rays (28; 29),

$$\vec{f} = \frac{n_1 P}{c}\left[\hat{i}_0 - (R_0\hat{r}_0 + \frac{n_2}{n_1}T_0\hat{t}_0)\right] \tag{1.16}$$

where $\hat{r}_0$and $\hat{t}_0$ define the unit vectors along the reflected and transmitted directions, respectively. R_0 and T_0 represent the Fresnel reflection and transmission coefficients.

For optical fibers, the intensity of light emanating is best approximated by a Gaussian distribution. Thus, the power incident on a differential area Δs is related to the total beam power P_T by the following equation,

$$P = \left[\frac{2P_T}{\pi w^2} exp\left(-\frac{2r^2}{w^2}\right)\right]\Delta s\, cos\theta \tag{1.17}$$

where w and r represent the beam width and the radial distance from the beam axis $\hat{z}$ at the interacting point, and θ is the angle between the surface normal and the beam propagation direction. Using Eq. (1.16) and (1.17) the surface stress can be shown to be

$$\vec{\sigma} = \frac{n_1 cos\theta}{c}\left[\hat{i}_0 - (R_0\hat{r}_0 + \frac{n_2}{n_1}T_0\hat{t}_0)\right]\left[\frac{2P_T}{\pi w^2} exp\left(-\frac{2r^2}{w^2}\right)\right] \tag{1.18}$$

In the case of a close object, a transmitted beam experiences multiple internal reflections. If we consider m internal reflections, the total optical surface stress is

$$\vec{\sigma}_m = \frac{2P_T n_1 T_0 \Delta s cos\theta}{\pi w^2 c \Delta s_m} exp\left(-\frac{2r^2}{w^2}\right)\prod_{j=1}^{m-1} R_j\left[\frac{n_2}{n_1}\hat{i}_m - (\frac{n_2}{n_1}R_m\hat{r}_m + T_m\hat{t}_m)\right] \tag{1.19}$$

The incident vector takes into account the divergence of the beam, meanwhile the subsequent reflected and transmitted vectors can be computed using Snell's law. Finally,

the total force is the integral of the stress over the surface.

1.1.4 Thermal Gradient force

In a material that possesses a complex dielectric constant, the absorption of electromagnetic energy induces a change in temperature which leads to a convective force due to the fluid flow.

The dynamics of such a system can be studied by numerically solving the steady-state, incompressible Navier-Stokes equation in the microfluidic environment together with a heat transfer equation. The incompressible Navier-Stokes equations consist of a momentum balance

$$\rho\frac{\partial u}{\partial t} + \rho u \cdot \nabla u = -\nabla p + \eta\nabla^2 u + F \tag{1.20}$$

This equation ignores variations in density with temperature. We add free convection to the fluid flow with the Boussinesq approximation: $F = -g(\rho(T) - \rho(T_0))$. We assume that the fluid density ρ is independent of pressure and depends linearly on the temperature T: $\rho - \rho_0 = -\rho_0 C_p(T - T_0)$, where C_p is the heat capacity.

The heat equation is an energy conservation equation. The change in energy is equal to the heat source minus the divergence of the diffusive heat flux

$$\rho C_p\left(\frac{\partial T}{\partial t} + u \cdot \nabla T\right) + \nabla \cdot (-k\nabla T) = Q \tag{1.21}$$

where Q is a source term. The solution of the coupled system provides the velocity field and temperature distribution within the fluid.

This effect is important for systems with absorption. A numerical simulation estimates that, for a 1 μ m particle, the convective force is $\sim 1 \times 10^{-6}$ pN for the channel and parameters used in this thesis.

Chapter 2

Light Assisted template self-assembly

Self-assembly methods (2) have been used to construct complex materials including three dimensional photonic crystals (30). However, a fundamental constraint is that only energetically favorable structures are formed. To overcome this problem, templated self-assembly methods have been introduced (3; 4). The template guides particle arrangement, allowing the formation of diverse albeit static crystal structures. Here we consider how optical forces can be used to direct assembly and reconfiguration of particles on a photonic crystal slab, which serves as an optically reconfigurable template. Our calculations predict the formation of stably trapped crystal patterns that depend on the wavelength and polarization of the light source. We envision that the process of light-assisted templated self-assembly may be used for fabrication of complex photonic materials and all-optically reconfigurable photonic devices.

Optical forces have been studied extensively since the discovery of optical tweezers (5; 6). While standard optical tweezers use a focused laser beam to trap and manipulate particles, structured light fields (14; 15) allow even greater control over particle deflection, transport, and sorting. Recently, researchers have used light fields near microphotonic devices to trap and manipulate particles. This work leverages the strong electromagnetic gradients near devices such as nanoapertures (7), gratings (8), photonic-crystal microcavities (9; 10) to generate large optical forces. However, much of this work has considered single-particle traps.

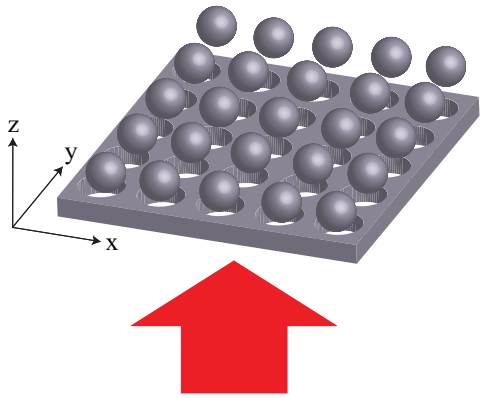

Figure 2.1: Light-assisted templated self-assembly using a photonic crystal slab

Here we suggest the possibility of assembling multi-particle patterns. We propose to use the guided resonance modes of photonic crystal slabs (17) to enhance the optical forces acting upon particles in a solution. In contrast to previous work on Fabry-Perot enhancement of trapping forces above a flat substrate (16), the photonic crystal is used to form spatially distinct trapping patterns at different polarizations and wavelengths. While previous work has examined light forces between different layers of particles in colloidal photonic crystals (22), forces on colloidal layers above a microfabricated template were not considered.

The system we consider is shown schematically in Fig 2.1. In an experiment, light would illuminate the photonic crystal slab from below. The structured light fields above the slab give rise to optical forces on particles in a solution, which can potentially result in trapping. Due to the variation of the electromagnetic field over spatial length scales comparable to the particle diameter, the dipole approximation cannot be assumed. However, the optical force can be found by using full-vectorial calculations of Maxwells equations to calculate the Maxwell Stress Tensor (22).

2.1 Design

For concreteness, we consider a silicon photonic crystal (ϵ = 11.9) with a square lattice of holes of radius $0.2a$ and thickness $0.6a$ resting on a silica substrate (ϵ = 2.1), where a is the lattice constant of the photonic crystal. The holes in the photonic crystal and the region above the crystal are filled with water (ϵ = 1.77). The incident light is an x-polarized plane wave propagating in the z direction.

We calculate the transmission through the slab numerically using the finite-difference time-domain (FDTD) method (31) with the freely available MIT MEEP package (32). The computational resolution is 32 grid points per lattice constant. Fig 2.2(a) shows the normalized transmission through the photonic-crystal slab. The transmission exhibits three distinctive resonance peaks at frequencies $\nu(c/a)$ = 0.4721, 0.4958, and 0.5008. The characteristic shape of the resonance peaks is well known from existing work in literature (17). We will refer to the three resonances shown as R1, R2, and R3 respectively.

2.2 Optical force using guided modes

We calculate the force on polystyrene spheres (ϵ = 2.28) of radius $0.1a$. The center of the sphere is placed at a height of $0.25a$ above the slab surface. We calculate the Maxwell stress tensor on the surface of an integration box of size $0.3a$ centered on the particle (23). The calculation is done in a computational cell that includes one period of the photonic crystal slab. Periodic boundary conditions are used in the lateral directions (x and y), and perfectly matched layer boundaries are used in the z direction. The forces calculated in this manner represent the optical forces on a periodic array of polystyrene

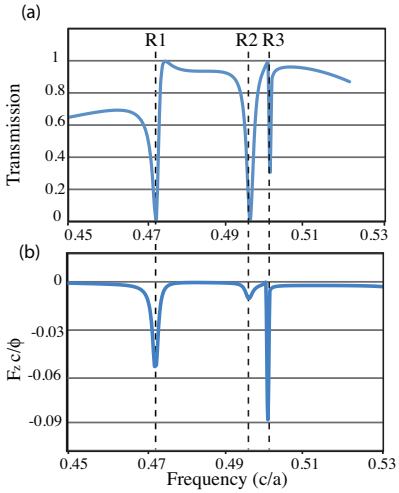

Figure 2.2: (a) Normalized transmission of a silicon slab on a silica substrate for a height of $0.6a$ and hole radius of $0.2a$, (b) Force in the z direction for a sphere of radius $0.1a$ placed $0.25a$ above the slab surface. The sphere is positioned equidistant from the four closest holes.

spheres above the photonic crystal slab.

We plot the dimensionless quantity $F_z c/\phi$, where F_z is the z component of the optical force, ϕ is the incident power per unit cell and c is the speed of light (see Fig 2.2(b)) for a sphere positioned equidistant from the four closest holes. For each of the three resonance frequencies shown in Fig 2.2(a), we observe a peak in the optical force. The sign of the force is negative, indicating that the particles are attracted toward the slab. For comparison, we calculate the radiation pressure of a plane wave on a spherical particle in the absence of the photonic crystal. We obtain a repulsive force of $F_z c/\phi \sim 1 \times 10^{-5}$, three orders of magnitude smaller than the attractive optical force above the photonic crystal. We expect that even larger optical forces can be achieved by using a photonic-crystal slab with higher-Q resonances. Higher Q has been correlated with decreasing hole size (17).

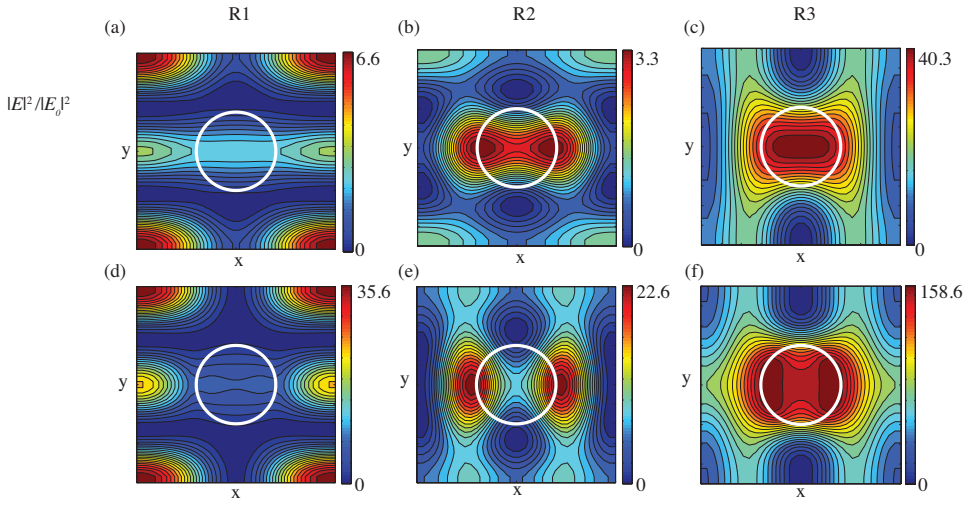

Figure 2.3: Normalized intensity for normally incident x-polarized light for R1, R2, and R3, respectively at a height of (a-c) $0.25a$ above the surface of the slab and (d-f) $0.1a$ above the surface of the slab. White circles indicate hole positions.

The intensity for these resonances is shown in Fig. 2.3(a-c) at a height of $0.25a$ above the surface of the slab. Fig 2.3(d-f) shows the intensity at a height of $0.1a$ (equal to the particle radius). The intensity $|E|^2$ is normalized to the source intensity $|E_0|^2$. We observe that each resonance has a different field profile. There is a slight change in field profile with height, and the intensity increases as you approach the slab.

2.3 Optical force maps and reconfiguration

We now look at the spatial dependence of the force on resonance. The force at each point is calculated by placing the sphere at that point, calculating the full-vectorial electromagnetic fields, and computing the Maxwell Stress Tensor. For numerical reasons, we have calculated the forces at a height of $0.25a$ above the slab to insure that the Maxwell Stress Tensor integration surface does not overlap with either the particle or the slab boundaries. Figs 2.4(a), (b), and (c) show the force on a vertical (x-z) slice

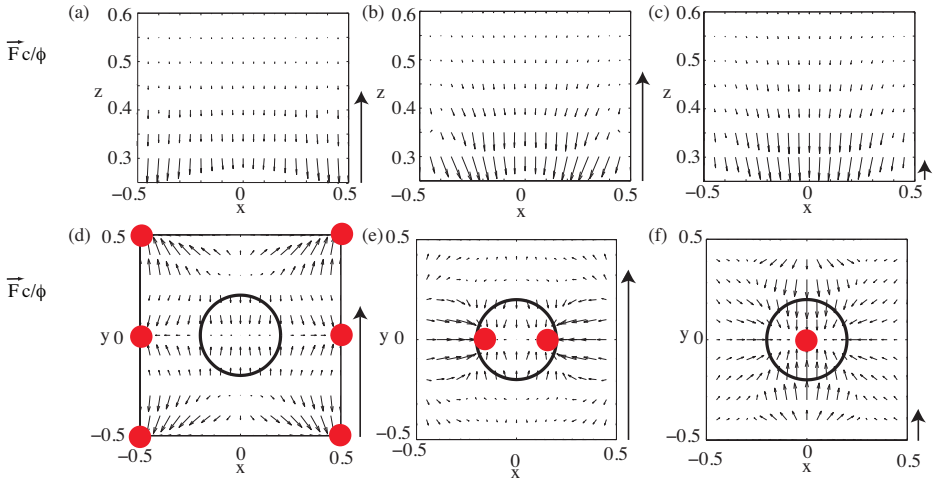

Figure 2.4: (a-c) Force in the x-z plane at y = 0, (d-f) Force in the x-y plane at z = 0.25a for R1, R2, and R3, respectively. The red dots represent stable trapping points and the black circles indicate hole positions.

at y=0. The length of the arrows next to the graphs represents a value $Fc/\phi = 0.2$. The vertical forces are attractive over the whole unit cell: this indicates that a particle near the slab will be attracted to it.

Figs 2.4(d), (e), and (f) show the force on a horizontal (x-y) slice 0.25a above the slab surface. The circles indicate hole positions. The arrows next to the graphs represent a value of $Fc/\phi = 0.2$, and the red circles represent the stable points to which the particles are attracted. R1, R2 and R3 correspond to different stable patterns. Fig 2.4(d) has an additional stable point at the center of the unit cell, but it is not labeled with a red dot because it has a weak lateral force compared to other trapping points. Similarly, Fig 2.4(e) has two additional weakly stable points at the bottom (or top) edge of the unit cell. We note that the spatial profile of the forces exerted on particles touching the slab surface (height 0.1a) may differ slightly from those shown here due to the weak variation in intensity with height (Fig 2.3).

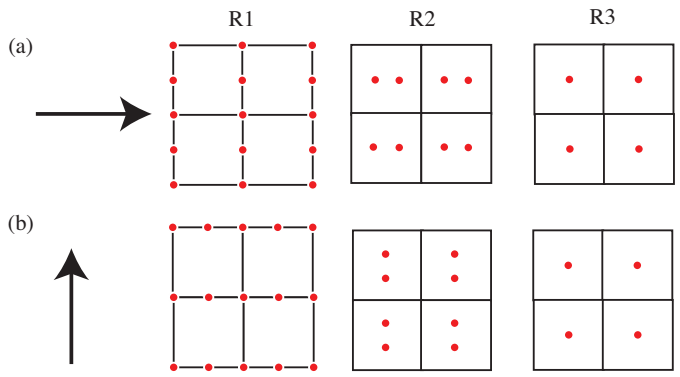

Figure 2.5: (a) Pattern for x-polarization, (b) Pattern for y-polarization.

Different light polarizations correspond to different self-assembled patterns, as shown in Fig 2.5. Due to the symmetry of the photonic crystal, the patterns for y-polarized light are the same as those for x-polarized light, only rotated $\pi/2$ (Figs 2.5(a) and 2.5(b)).

In an experiment, particles may be trapped one by one, or a few at a time, in order to build up ordered patterns. We believe that the red dots shown in Figs 2.4 and 2.5 are good predictors of the patterns that will be formed in this manner. In our computations, due to the boundary conditions on the unit cell, we are calculating the optical force on periodic arrays of particles above the photonic crystal slab. However, since interparticle interactions (27) are negligible in this system, the force on an individual particle above the slab will be nearly identical.

2.4 Inter-particle interaction

To show that interparticle interactions are weak compared to the force on a particle from the photonic crystal, we considered the geometry shown in Fig 2.6(a). A first

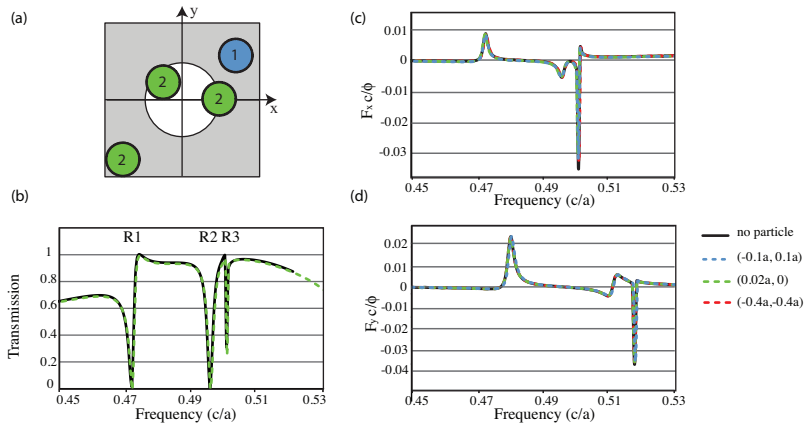

Figure 2.6: (a) Schematic of the system (b) Transmission spectrum of photonic-crystal slab with and without particles above (c) $F_x c/\phi$ on particle 1 for 3 different positions of particle 2 (d) $F_y c/\phi$ on particle 1 for 3 different positions of particle 2. The legend indicates the position of particle 2 in (b), (c), and (d).

particle (labeled 1, blue circle) was placed over the slab at a position of [$0.3a$, $0.3a$, $0.25a$]. A second particle was placed in one of three alternate positions (labeled 2, green circles). Fig 2.6(b) shows that the presence of the particles does not visibly affect the transmission spectrum. In Figs 2.6(c) and (d), we plot the lateral forces on particle 1 for different positions of particle 2. It can be seen that particle 2 has minimal effect on the force.

As an additional check, we recalculated the force maps of Figs 2.4(d-f) using a larger computational cell of size $2a \times 2a$, with one particle per computational cell. No changes were observed in the force maps.

Lastly, we checked that when particles were placed at each of the red dots in Fig 2.4(d-f), the configuration remained stable despite the perturbation. One particle per unit cell was displaced, and We verified that the restoring force was in the necessary direction to restore the initial pattern.

In the system studied here, the particles do not significantly affect the transmission spectrum (Fig 2.6(b)). We have checked that even if the particles are placed inside the holes in the slab or on the slab surface, the shift in the resonance is a small fraction of the resonance width (15% or less). For larger particles, particles of higher index, and/or higher Q slab resonances, particle trapping may begin to shift the resonance position. This opens up the possibility for intriguing phenomena such as self-induced or bistable trapping, effects which have previously been studied for particle trapping near photonic cavities (9). This is an interesting direction for further research.

2.5 Parametric dependency

Fig 2.7(a) shows the vertical force as a function of the dielectric permittivity of the sphere, ϵ, for a sphere of radius $0.15a$. The magnitude of the force increases with ϵ, and no shift is observed in the resonance peak. Similarly, Fig 2.7(b) shows the vertical force as a function of sphere radius for a particle with $\epsilon = 3$. The force increases with increasing sphere radius and no shift is observed in the resonance peak. For larger sphere radii, increasing ϵ will increase the force and shift the resonance peak, as shown in Fig 2.7(c). The figure shows the region of the spectrum near R1 for a sphere radius of $0.35a$.

Changing the template will change the frequencies and quality factors of the resonances, thus changing the optical force. Fig 2.8(a) shows the change in force due to changing hole diameter for R1, $\epsilon = 2.28$, slab thickness $0.6a$ and sphere radius of $0.1a$. The force peak shifts to higher frequencies as d is increased. The force peak widens, and the peak amplitude decreases, corresponding to a decrease in the resonance quality factor. Fig 2.8(b) shows the change in force with slab thickness for R1, $\epsilon = 2.28$, hole

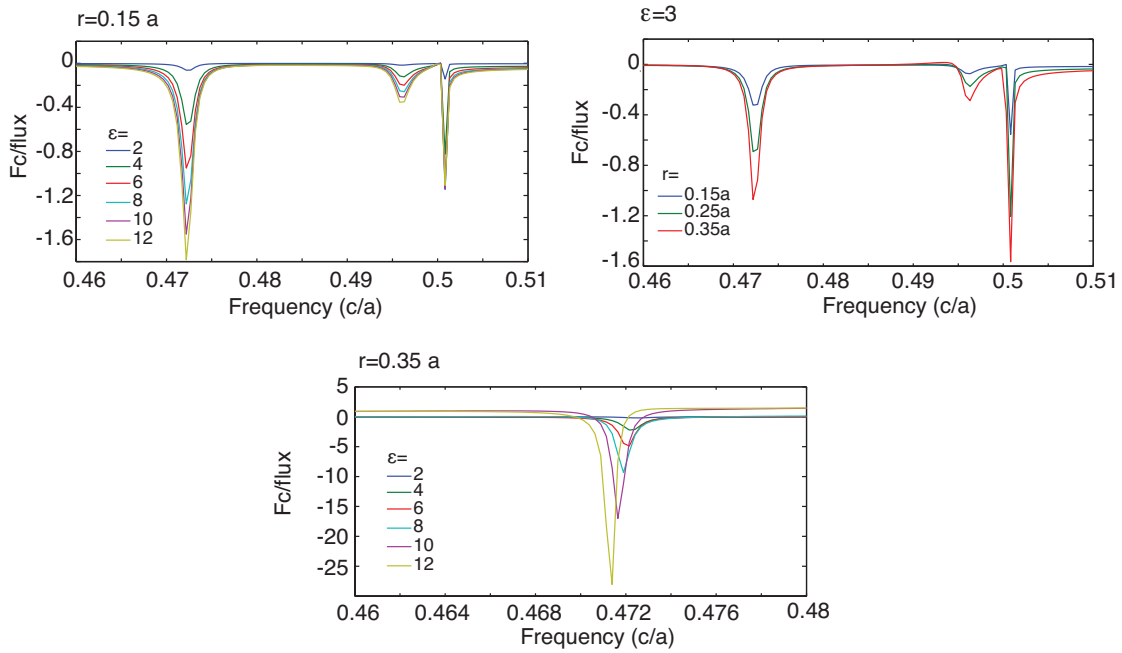

Figure 2.7: (a) Vertical force as a function of ϵ for a sphere with radius $0.15a$, (b) vertical force as a function of sphere radius for ϵ=3, (c) Vertical force for R1 as a function of ϵ for a sphere radius of $0.35a$.

diameter of $0.4a$, and sphere radius of $0.1a$.

2.6 Experimental considerations

The photonic-crystal slabs studied here are fabricated in a silicon-on-insulator wafer using standard techniques (33). The lattice constant of the photonic crystal can be scaled to place a given guided resonance at a particular wavelength of interest (1). For a = 760nm, for example, R1 occurs at λ = 1609 nm, while R2 occurs at 1532 nm. For a= 375 nm, R1 is at 794 nm and R2 is at 748 nm. An upper bound on the power required for trapping was obtained by setting the height of the potential depth $|\Delta U| >$

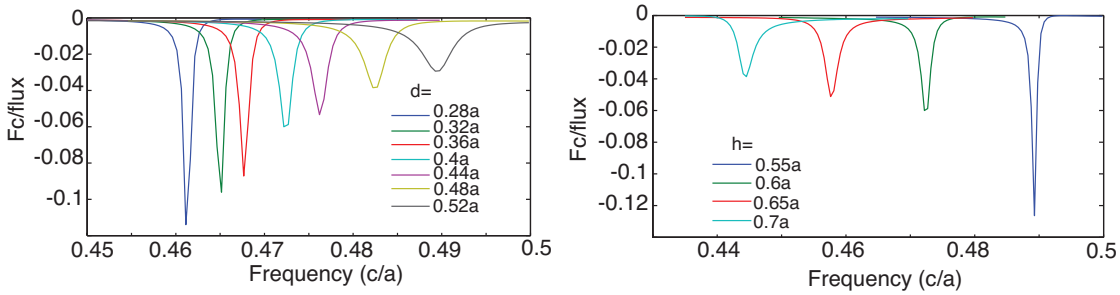

Figure 2.8: (a) Vertical force as a function of ϵ for a sphere with radius $0.15a$, (b) vertical force as a function of sphere radius for ϵ=3, (c) Vertical force for R1 as a function of ϵ for a sphere radius of $0.35a$.

10 K_BT. The power density for a = 760 nm was 1 mW/unit cell for R1, which has a modest Q of $\sim$260. The required power decreases with increasing Q. Moreover, the power calculated in this manner is likely to be overestimated. Our results indicate that the particles will be attracted to the surface of the slab. As seen in Fig 2.3, the intensity increases closer to the slab surface, producing a higher force than the values shown in Fig 2.4, which were calculated for a height of $0.25a$ (for a particle touching the slab surface, with a height of $0.1a$).

In conclusion, we predict that optical forces above photonic crystal slabs will lead to a variety of complex, stably trapped crystal patterns. Changing the wavelength or polarization of the incident light may be used to reconfigure the patterns. We expect the approach of light-assisted self-assembly, described here, to be of broad utility for fabrication of complex photonic materials, sensors, and filters. It is intriguing to consider whether metamaterials based on metal nanoclusters (34), for example, could be assembled in the manner we describe, using the optical response of the nanoclusters to tune or adjust assembly.

Chapter 3

Experimental demonstration of Light Assisted Template Self-assembly

In this chapter, we demonstrate for the first time the trapping of multiple particles using an extended mode in a two-dimensional photonic crystal slab. Our system improves upon previous optical trapping work in three main ways. First, we have demonstrated a compact, multiparticle trapping system in the present work; over 180 particles are trapped in an area less than 150 μm^2. The number of particles could be increased in a straightforward way by proper design of the structure or by increasing the size of the incident beam. Second, since the large array of particles is trapped by exciting a single mode of the structure without the use of a spatial light modulator or any movement of the beam or sample, it can be easily adapted for a variety of integrated, lab-on-a-chip applications. Finally, by tuning the polarization of the incident light, we can tune the preferential direction of the in-plane trapping stiffness of our structure.

The process of light-assisted templated self-assembly (LATS) is shown schematically in Fig 3.1. Light is incident from below on a photonic-crystal slab. The photonic-crystal slab consists of a silicon device layer patterned with a periodic array of air holes. The slab supports guided-resonance modes, electromagnetic modes for which the light intensity near the slab is strongly enhanced. In previous work (35; 36), we have predicted theoretically that when the incident laser is tuned to the wavelength of a guided-resonance mode, nanoparticles will be attracted toward the slab. The

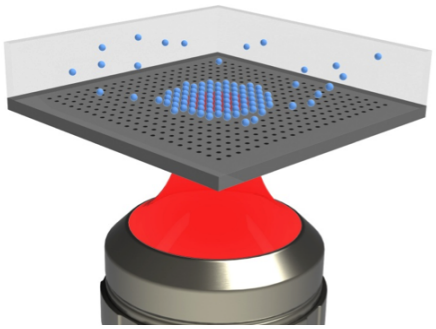

Figure 3.1: Schematic picture of templated, light-assisted self assembly. Incident light from below excites a guided-resonance mode of a photonic-crystal slab, giving rise to optical forces on nanoparticles in a solution. Under the influence of the forces, the nanoparticles self assemble into regular patterns.

attractive, optical force arises from a strong electric field gradient just above the slab surface. In addition, the nanoparticles will experience lateral optical forces due to the electromagnetic field structure of the guided mode. We expect the optical forces to result in the assembly of particles into regular 2D arrays. Importantly, the array patterns formed can be different from the triangular, close-packed structure formed by traditional, colloidal, self assembly. Figure 1 depicts a square array of particles, as one example. By exciting different resonant modes of the slab, or by designing different slab templates, we expect that a variety of patterns can be produced. Moreover, these patterns can reversibly be assembled or disassembled, suggesting the possibility of ”programmable optical matter”.

3.1 Design

We designed, fabricated, and characterized a photonic-crystal slab for use in the LATS process. An electron micrograph is shown in Fig 3.2(a). The device was fabricated in silicon using electron-beam lithography and reactive ion etching (see Methods

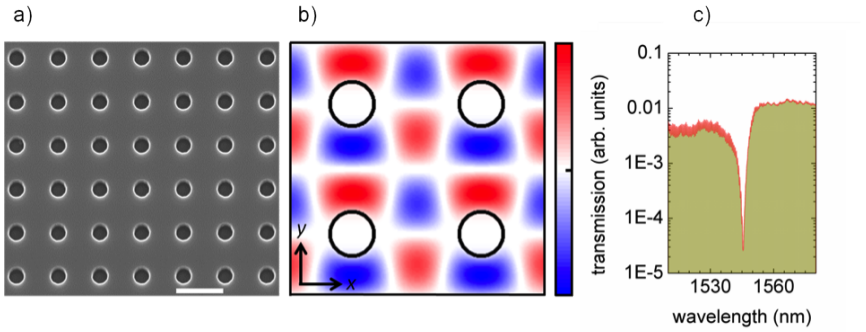

Figure 3.2: (a) SEM image of photonic-crystal slab. The scale bar in the inset is 1 μm. (b) 3D FDTD simulation of the magnetic field (H_z) for a normally-incident, x-polarized plane wave. Circles represent the positions of holes; four unit cells are shown. (c) Measured transmission spectrum (log scale).

in Sec. 3.4). The dimension and spacing of the holes were designed to support doubly-degenerate guided-resonance modes near 1.55 μm. The magnetic field profile resulting from an x-polarized, incident plane wave is shown in Fig 3.2(b). Fields were calculated using the three-dimensional finite-difference time-domain method (FDTD). The field-profile for a y-polarized incident wave is rotated by 90 degrees. Fig 3.2(c) shows the measured transmission spectrum of the device. The guided-resonance mode appears as a dip in the spectrum. The quality factor, Q, was determined to be $\sim$ 170 by fitting to a Fano-resonance shape.

3.2 Results

We carried out the assembly process in a microfluidic chamber filled with 520-nm diameter polystyrene particles, using a laser power of 64 mW. Fig 3.3 shows snapshots of the LATS process. The photonic-crystal lattice is visible in the background of each frame. When the laser beam is turned on, nanoparticles are attracted towards the slab, and begin to occupy sites within the square lattice (Fig 3.3(a)). As time progresses,

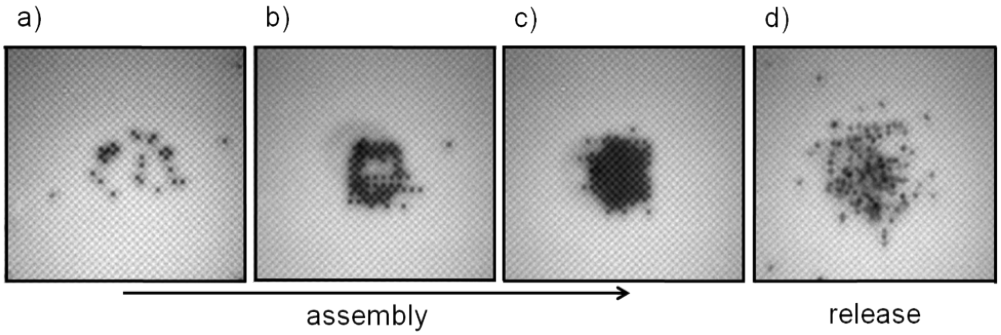

Figure 3.3: Light-assisted, templated self assembly of 520 nm diameter particles above a photonic-crystal slab. The square lattice of the slab is visible in the background, oriented at 45 with respect to the camera. (a-c) Sequential snapshots taken with the light beam on. (d) Snapshot taken after the beam is turned off.

additional particles diffuse into the region where the beam intensity is high, and begin to form a cluster (Fig 3.3(b)). Eventually, a regular array of particles is formed (Fig 3.3(c)). The square symmetry of the assembled particles is evident from the picture. When the laser beam is turned off, the particles immediately begin to disperse and diffuse away from the slab (Fig 3.3(d)). The frames in Fig 3.3 were recorded with a dilute particle solution for clarity of imaging, and represent an elapsed time of approximately one hour. Faster cluster formation occurs within solutions of higher particle concentration.

Each site of the square lattice may be viewed as an optical trap. We used particle-tracking software to analyze particle motion for fully-assembled clusters (see Sec. 3.4). Fig 3.4 shows the recorded particle positions extracted from a 20-second video. The incident light was polarized along the x-direction of the lattice. The figure shows that the particles tend to stay above the holes in the photonic crystal, with some variation in position over time. Each blue ellipse represents a fit to the data in a single unit cell. It can be seen that the variation in particle position increases at the edge of the trapping

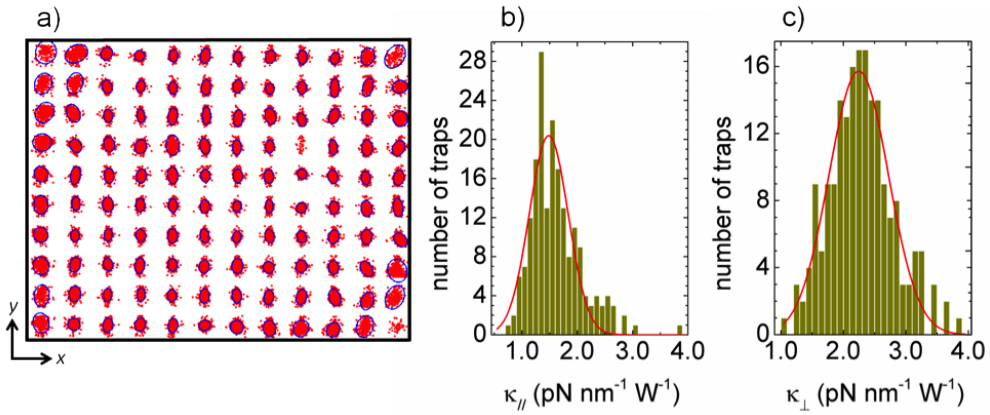

Figure 3.4: Trap stiffness for incident, x-polarized light. (a) Particle positions (red dots) extracted from a 20-second video. Blue ellipses represent two standard deviations in position. (b) Histogram of stiffness values in the direction parallel to the polarization of the incident light. (c) Stiffness in the direction perpendicular to the incident polarization.

Angle	κ_x(pN nm^{-1} W^{-1})	σ_x	κ_y(pN nm^{-1} W^{-1}	σ_y
0^0	1.48	0.35	2.25	0.48
45^0	1.88	0.52	1.79	0.46
90^0	2.08	0.40	1.39	0.29

Table 3.1: Polarization dependence of trap stiffness.

region, due to the reduction in power away from the center of the beam.

The stiffness of each trap can be determined from the variance in particle position (37). Figs 3.4(b) and 3.4(c) show histograms of the in-plane stiffness values extracted from the videos. The stiffness of each trap was normalized to the local intensity in that unit cell (see Sec. 3.4). We observe that the power-normalized stiffness over the array of traps is normally distributed, both for the parallel and perpendicular stiffness. The mean parallel stiffness is lower than the perpendicular stiffness, as shown in Table 3.1 (0^o angle).

We observe that the trap stiffness can be tuned by rotating the direction of incident light. When the incident light is polarized at 45^o with respect to the lattice directions, the stiffness values are approximately the same in the x- and y-directions (Table 3.1). This is to be expected, since the incident light excites both of the doubly-degenerate modes with equal strength. At 90^o, the stiffness in the perpendicular direction (y) is again lower than in the parallel (x) direction. The ability to tune the stiffness with incident light indicates the strong optical nature of our traps. The mean values of stiffness are comparable to those reported elsewhere in the literature for single particle traps (38).

Using the Stokes drag method (see Sec. 3.4), we experimentally estimated the maximum force exerted on the particles by the traps to be 0.3 pN.

3.3 Discussion

To understand how the optical forces result in the observed nanoparticle patterns, we calculated the force numerically (see Sec. 3.4). Fig 3.5(a) shows the force on a 520 nm diameter particle whose bottom edge is 25 nm above the surface of the photonic crystal slab for x-polarized light. The background color represents the vertical force, where a negative force indicates attraction toward the slab. There are two regions above and below the hole where the force is slightly repulsive, but at any other position within the unit cell the particle results in attraction towards the slab. The arrows represent in-plane forces.

To determine the equilibrium position of the trapped particle, we calculate the optical potential. Given the relative size of the particles (260 nm radius) and holes (150

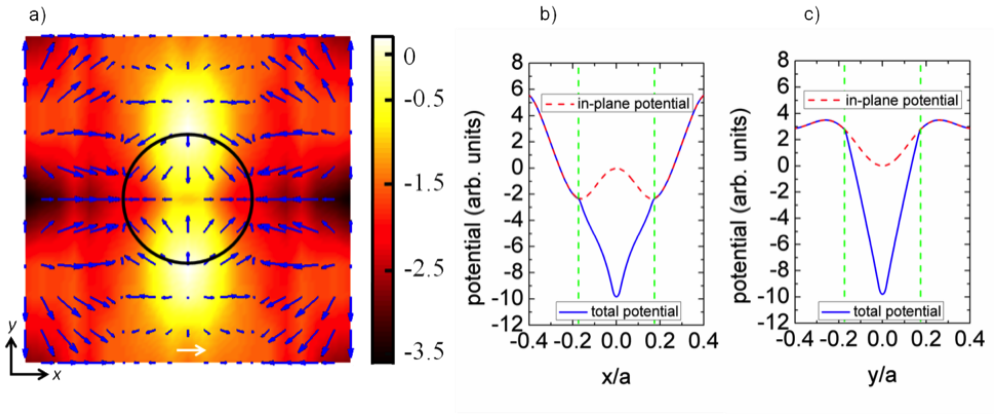

Figure 3.5: (a) Force map in one unit cell. The black circle represents the position of a hole, and the color bar represents the vertical optical force in dimensionless units of Fc/P, where c is the speed of light, and P is the incident optical power. A negative force indicates attraction toward the slab. The arrows represent the magnitude of the lateral optical force. The length of the white arrow at the bottom center of the figure corresponds to the maximum in-plane value of 1.6. (b) The potential through the center of the hole along the x-direction. The green dashed lines indicate the position of the hole. (c) The potential through the center of the hole along the y-direction.

nm radius) in our experiment, the particle can be drawn into the hole by the attractive vertical force. We calculate the optical potential as a function of x-y position. For each x-y position, the vertical height of the particle is as small as possible, given the geometrical constraints (see inset in Fig 3.5(b)). The result is shown by the blue line (total potential) in Figs 3.5(b) and 3.5(c). It can be seen that the stable equilibrium position is at the center of the hole (x = 0, y = 0), in agreement with experimental observations.

The ability of the particle to sink into the hole is a key factor in determining the equilibrium positions. For comparison, the red, dashed line (in-plane potential) in Fig 3.5(b) shows the optical potential calculated at a constant z height (bottom edge of particle 25 nm above the slab surface). Two local minima are observed at the edges of the hole, which are indicated by green, dashed lines. From inspection of Fig 3.5(a), it

can be seen that these points correspond to locations where the in-plane forces are zero. However, these two minima are not stable equilibrium positions of the total potential, (blue line, Fig 3.5(b-c)).

From our experiments, we determined that the threshold intensity for trapping was 134 μW per unit cell (see Sec. 3.4). For this intensity, the calculated potential depth is 4.5 $k_B T$.

3.4 Methods

3.4.1 Fabrication

The photonic-crystal device consists of a square lattice of holes etched into a SOI wafer. The lattice constant a is 860 nm, and the hole radius is 0.174a (150 nm). The thickness of the silicon device layer is 250 nm. The buried oxide layer is 3 μm thick, and the silicon substrate is 600 μm thick. To fabricate the device, a layer of PMMA 4$\%$ in anisole was spin coated onto an SOI wafer. Electron beam lithography at 30 kV was used to write the photonic-crystal pattern into the resist. A modified Bosch process was used to transfer the pattern into the Si device layer using a mixture of SF6 and C4F8 gases. Plasma-enhanced chemical vapor deposition was used to deposit a 193 nm layer of SiNx onto the polished, back surface of the sample to reduce unwanted reflections.

The photonic-crystal sample is mounted on a circular glass slide and inserted in a rotary stage. The sample is covered with a solution of 520 nm diameter polystyrene particles (700 μL of Thermo Scientific Fluoro-Max R520 particles in suspension, diluted in 60 mL of deionized water). 600 μL of 1$\%$ Triton-X was added to the solution to minimize particle stiction to the sample surface. On a second glass slide, an

open-topped microfluidic chamber (4 mm x 4 mm) was fabricated in a 5 μm layer of PDMS using photolithography. The PDMS chamber was pressed on to the sample and sealed inside the rotary stage.

3.4.2 Optical setup

A Santec tunable laser with a tuning range from 1500 nm to 1620 nm was connected to an erbium-doped fiber amplifier and a tunable bandpass filter with a width of 1 nm. An adjustable, neutral-density filter and polarization-control optics were used to control the power and polarization of the beam. A fiber-to-free-space collimator directed the beam to the entrance aperture of a 20X objective (NA = 0.26), which focused the beam onto the top surface of the sample from the back side. A second 20X objective was used in conjunction with a beam splitter to collect the light from the top surface and to image the particle motion on a CMOS camera. Prior to each self-assembly experiment, the transmission was measured in cross-polarization mode. Polarizers before and after the sample were oriented at 90 degrees from one another, and the wavelength of the transmission peak was identified. This laser was then tuned to the peak wavelength to carry out light-assisted self assembly.

3.4.3 Stiffness analysis

After the assembly of a cluster, we recorded videos with a fixed exposure time of 33 ms, the fastest value available in our experimental set-up. Typical videos were 600 or more frames in length. Particle motion was analyzed using MATLAB algorithms written by Blair and Dufresne (http://physics.georgetown.edu/matlab/), which are modified

versions of IDL routines written by Crocker and Grier (39).

The blue ellipses in Fig LATS2-4(a) are obtained by fitting the data in each unit cell. The direction and relative lengths of the major and minor axis are determined from the eigenvectors and eigenvalues of the scaled covariance matrix. The ellipse is drawn to represent a 95$\%$ confidence interval: positions outside the ellipse will be observed only 5$\%$ of the time by chance if the underlying distribution is Gaussian.

The measured variances were corrected for motion blur due to the finite integration time of the camera (40). We observed that the variance as a function of position within the cluster had a 2D Gaussian distribution. This is to be expected due to the spatial variation in intensity in the incident beam. We confirmed via 3D-FDTD simulations of a finite-size structure with Gaussian beam excitation that the field intensity above the slab has a Gaussian envelope. The stiffness values shown in Fig LATS2-4 are normalized to the local power at each trapping site, as determined by fitting the experimentally-measured variances to a 2D spatial Gaussian.

We directly measured the diffusion coefficient by first assembling a cluster, then blocking the beam and performing a linear regression fit to the subsequent diffusion as a function of time (39). A value of 0.56 $\mu m^2/s$ was obtained.

3.4.4 Force measurement

After assembling a cluster, we increased the flow speed until all particles were released. We observed the release of the last, trapped particle at a fluid velocity of 30 $\mu m/s$ for a laser power of 64 mW. In the low Reynolds number regime, the particle velocity v is

related to the external force by the equation $F = 6\pi\eta r v$, where η is the viscosity of the medium, and r is the radius of the particle.

3.4.5 Force and potential calculation

For each particle position within the unit cell, we performed an FDTD simulation to calculate the electromagnetic fields and obtained the optical force from an integral of the Maxwell Stress Tensor over a box just large enough to include the particle. The z dependence of the force inside the hole was obtained from an exponential fit to the field intensity above the slab. The power threshold for stable trapping was determined experimentally from the size of the stable cluster (16 unit cells, or 13.8 μm, in diameter). The Gaussian distribution of energy in the mode, obtained from a fit of the variance measurements, had a FWHM of 17 μm. Given the input power of 64 mW we find a peak intensity of 240 μW per unit cell, and a trapping threshold intensity at the edge of the cluster of 134 μW per unit cell.

3.5 Conclusions

In summary, we have demonstrated the technique that we term light-assisted, templated self-assembly. A square array of $\sim$ 180 polystyrene particles was assembled above a square-lattice photonic crystal. The assembly of the array resulted from the near field of an extended mode in a photonic crystal slab. The optical force was enhanced at the resonant frequency of the mode. We characterized the trapping stiffness of our system, and we showed that the calculation of optical forces successfully predicts the observed

equilibrium trapping positions.

Our system can be re-designed to assemble larger clusters. One approach would involve using a mode with a higher quality factor. The optical force scales with field intensity, and higher-Q modes should have higher local field intensity in the near field for a given input power. Furthermore, photons in higher-Q modes spread out further within the slab due to their longer lifetimes, thereby increasing the trapping area. Another approach is to re-design the photonic-crystal slab to increase the field concentration, as shown previously (36). Expanding or re-shaping the incident beam may also permit the formation of larger clusters.

One major advantage of our approach to self-assembly is the ability to assemble complex structures with symmetries that are not usually available due to energy concerns; here we have demonstrated just one. Different photonic-crystal templates will lead to different particle patterns and more complex unit cells. For a given template the particle patterns can be reconfigured by changing the wavelength or polarization of the incident beam. The nature of the particle itself can also be changed; interesting applications may result from the use of metal nanoparticles, quantum dots or combinations of different species (35).

Our system also lends itself to compact integration on-chip. The only external component in our experiment is the laser beam, and by fabricating the device in an active material, the source itself could also be integrated. Using electrical excitation of such a photonic-crystal laser would further miniaturize our structure in a way that would enable a variety of interesting on-chip applications.

We also anticipate that our technique will find applications in the fabrication of metamaterials and other photonic devices. After assembling a 2D array of particles, polymerization could be used to transfer the array to another substrate. The technique could thus be used to create 3D arrays layer-by-layer. With suitable design of the structure it should also be possible to assemble 3D arrays in situ.

Finally, a variety of dynamic, real-time applications could be enabled by LATS. For instance, LATS could be used to form reconfigurable photonic materials, such as a tunable photonic filter. The pattern of particles assembled can be altered in a reversible way simply by changing the input polarization or wavelength. By combining the optical potential landscape with microfluidic flow channels, it should also be possible to sort particles into different channels based upon size or refractive index (18; 19). The manipulation of biological objects could be simplified in our system by allowing for batch processing of tasks which typically use a single optical trap to examine a single specimen. Furthermore, by trapping biological objects with controlled spacing, our system allows for control over interactions.

Chapter 4

Optical trapping of Metal-dielectric cluster near a micro-cavity

Optical trapping and manipulation of particles has been demonstrated in a large number of structures since the discovery of optical tweezers. Resonant structures have been of great interest for trapping, sorting and cooling of particles with different optical properties such as atoms (41), quantum dots (42), DNA (43), resonant particles (44; 45), and dielectric particles (46). Different mechanism are used to resonantly enhance the electromagnetic field near a structure, in particular, waveguides (47), ring resonators (48), nanoantennas (49; 50), plasmonic structures, photonic crystals and photonic crystals cavities (51; 52) are the most popular choices.

However, in the dipole approximation, the gradient force neglects the field redistribution inside the optical cavity due to the polarization of the trapped particle. In this chapter, I use a FDTD method to solve Maxwell equations and compute the Maxwell stress tensor for a gold particle on top of a micro-cavity. Next, I show a secondary trap formation due to the field redistribution around the trapped gold particle and present an optical induced metal-dielectric cluster formation.

4.1 Trapping of gold nano-particles

As mentioned before, in templated self-assembly methods the geometrical relation between template and particles mainly defines the final structure. Thus, cluster formation of particle with same geometry but different composition cannot be controlled independently. The use of optical forces for particle trapping allows for differential response based on composition, since dielectric and metal particles experience different optical forces.

Strong optical forces can be obtained from the field enhancement near microphotonic structures. In particular, the microcavity mode of a photonic crystal can be used to create a nanoparticle trap (9; 10). In this section we present a controllable formation of a metal/dielectric cluster. We propose to use optical forces on particles in a solution above a photonic-crystal microcavity and the field redistribution due to the presence of a trapped particle. First, The photonic-crystal microcavity forms an optical trap for gold nano-particles. Field enhancement near the trapped gold nanoparticle then forms secondary trapping sites for a pair of dielectric nanoparticles. The process allow optical driven formation of a well-defined metal/dielectric cluster.

In contrast to previous work on optical binding where clustering comes from interactions between dipoles (27), in this paper we are considering nondipolar colloidal particles. Therefore, a trapped gold nano-particle on a photonic crystal microcavity acts as an off-resonance plasmonic trap for dielectric particles instead of a dipole-like particle. While previous work has examined light forces on metallic particles (53; 54; 55), between metallic nano-particles (56), and forces due to plasmonic traps (45; 57), optical forces in a particle-like off-resonance plasmonic trap were not considered.

The structure we consider is shown in Fig 4.1(a). In an experiment, light would illuminate the photonic crystal microcavity from below. The photonic crystal is formed of a hexagonal lattice of holes in Si (n = 3.46). The lattice constant is 400 nm, the hole radius is 140 nm, and the thickness of the silicon slab is 200 nm. The microcavity is created by removing a hole and displacing its two nearest neighbors along the x direction outward by 8 nm (9). The photonic crystal rests on a SiO_2 substrate (n = 1.45), and the holes in the lattice and the region above the crystal are filled with water (n = 1.33).

The microcavity mode was simulated using the finite-difference time-domain method (FDTD). A y-polarized plane wave illuminates the microcavity from below. We take the computational cell to be 3.6 μm x 3.4 μm x 2 μm in size. PML boundary conditions were used. A microcavity resonance value of 226.9 THz and quality factor $Q \sim 60$ were obtained. The microcavity strongly enhances the electric field near the missing hole, and the field intensity is 80 times higher than without the microcavity in the midplane of the slab. The field intensity in $(V/m)^2$ is plotted in Fig. 4.1(b) for a source power of $1.84mW/\mu m^2$. The intensity decays by a factor of 30 at a height of 130 nm above the slab Fig 4.1(c). At this height, we have observed that the strongest local intensity is achieved slightly off resonance (f = 229.1 THz) Fig 4.1(d).

A gold nano-particle, far from the plasmon resonance, can be seen as particles with slow varying frequency dependent imaginary dielectric constant, when the size of the particle is bigger than the mean free path of the electrons in the metal (58; 59). However, when the particle size is comparable to the electric field variation of the optical trap, the force cannot be approximated as the sum of a gradient, scattering and absorption force due to the strong field redistribution. Therefore, in order to calculate

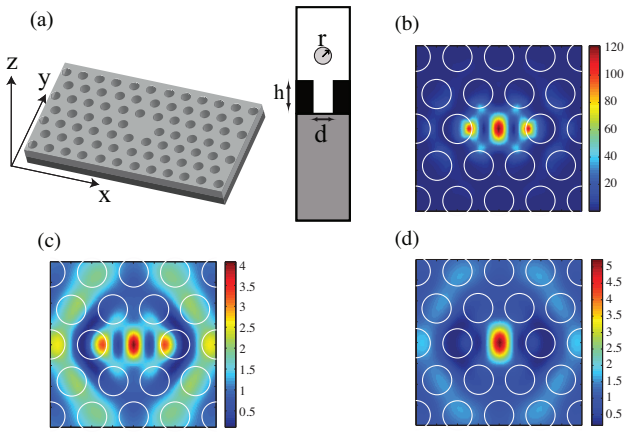

Figure 4.1: (a) Schematic of defect cavity in a hexagonal lattice of holes with diameter d and thickness h, (b) Electric field distribution at the center of the slab at resonance, (c) Electric field distribution at z=130 nm above the slab at resonance, (d) Electric field distribution at z= 130 nm above the slab slightly off resonance.

the optical force on spherical gold particles we used full-vectorial calculations of Maxwell's equations and the Maxwell Stress Tensor method (22).

In Fig 4.2, we plot the normalized optical force in the vertical direction for gold nanoparticles with several different radii. The bottom edge of each particle is 50 nm above the surface of the slab, and each particle is centered on the microcavity. F_z is the z component of the optical force, c is the speed of light in vacuum, and the flux is the total electromagnetic flux over the computational cell. A negative force indicates attraction toward the microcavity, whereas a positive force indicates repulsion. We observe both strong size and frequency dependence of the optical force near the microcavity resonance. For the largest gold particle shown (r = 160 nm), the force exhibits a Fano-resonance-like shape and is repulsive (positive force). For the smallest gold particle shown (r = 80nm), the force exhibits a single dip and is attractive (negative force). For particles of intermediate sizes, the force transforms from a Fano shape to a single dip. Thus, only gold particles with radii smaller than 160 nm can be trapped. Furthermore, the force on an 80nm gold particle is an order of magnitude larger than that felt by a

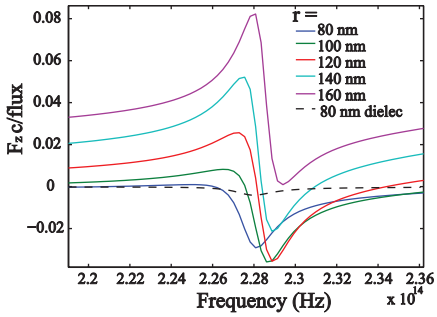

Figure 4.2: Vertical force on gold nanoparticles of different sizes and a dielectric particle with r = 80 nm and ϵ = 1.59.

dielectric particle of the same size.

Qualitatively, we can understand the different shapes of the curves in Fig 4.2 using insight from the dipole approximation. For trapping to occur, the attractive gradient force must be larger than the sum of the repulsive scattering and absorption forces. For small radii, the electric field polarizes the particle such that the gradient, scattering, and absorption contributions to the optical force can be written as (54):

$$F_{grad} = \frac{|\alpha|}{2}\nabla|E|^2 \tag{4.1}$$
$$F_{sca} = \frac{n_w \vec{s} C_{sca}}{c}$$
$$F_{abs} = \frac{n_w \vec{s} C_{abs}}{c}$$

From the analytical expressions in Ec (4.1) we plot the forces in Fig 4.3. It can easily be seen that the gradient force on a gold particle is attractive and has the form of a single dip near resonance, while the scattering and absorption forces are repulsive and have a Fano-like shape.

Looking at Fig 4.2, we observe that for small particles (e.g. r = 80 nm), the shape of the optical force curve resembles that of a gradient force term. For larger particles (e.g.

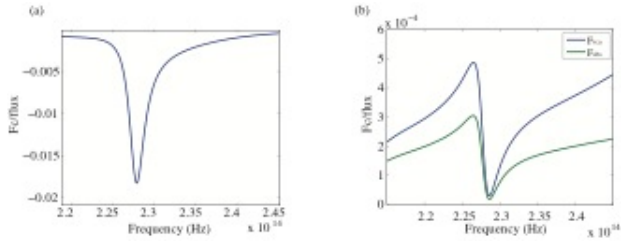

Figure 4.3: Gradient (a), and scattering and absorption forces (b) on a gold particle with r = 80nm using the dipole approximation.

r = 160 nm), the shape of the curve resembles that of scattering and absorption terms. We infer that as the particle size decreases, the gradient force dominates the scattering and absorption effects, leading to trapping.

In Fig 4.4, we plot the frequency-dependent vertical force on a gold particle with r = 80 nm for several different heights, assuming the particle is centered over the microcavity. The frequency at which the optical force peaks shifts as a function of particle height, due to the interaction between the gold particle and the microcavity. This effect is similar to the self-induced trapping effect previously observed for dielectric particles (9). For a frequency of 229.1THz, the force is attractive for all heights shown.

We fix the excitation frequency at 229.1THz and consider the spatial dependence of the optical force. In Figs 4.4(b) and 4.4(c), we show the normalized horizontal and vertical forces (Fc / flux) on a gold particle whose bottom edge is located 50nm above the slab. The color bars indicate the magnitude, and the arrows in Fig. 4.4(b) indicate the direction. There is a stable trapping position at the center of the microcavity. The trap is weakest along the y-direction and has a stiffness [10] k_y = 0.2 $pNnm^{-1}W^{-1}$. We estimate a minimum trapping power of 1mW by requiring the stability number to be at least one (60).

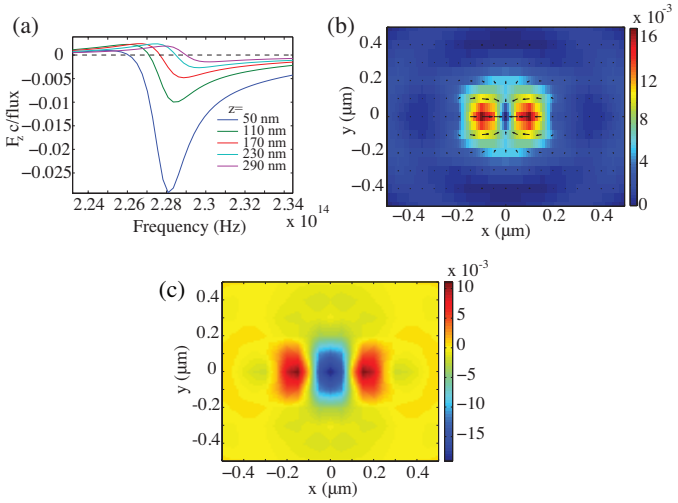

Figure 4.4: (a) Vertical force as a function of frequency for several different vertical positions. Normalized force in the (b) horizontal and (c) vertical directions as a function of position in the x-y plane for a gold particle with r = 80nm.

4.2 Cluster formation

A gold nanoparticle trapped at the center of the microcavity will redistribute the electromagnetic field, forming new optical trapping locations. Figs 4.5(a) and 4.5(b) show the electric field intensity 130nm above the slab at the fixed frequency of 229.1THz for the same source power as in Fig 4.1. The maximum value of intensity is 7 times higher than without a gold particle. The high intensity regions can attract dielectric particles. Figs 4.5(c) and 4.5(d) show the horizontal and vertical optical forces on a dielectric particle with n =1.59 and r = 80 nm in the presence of the trapped gold nanoparticle, indicated by the solid, yellow circle. The dielectric particle is stably trapped in the position indicated by the dashed circles. In the Figures, the arrows next to the graphs represent values of Fc / flux = 0.002. We estimate a minimum trapping power of 7 mW with trapping stiffnesses of $k_x = 0.08\ pNnm^{-1}W^{-1}$, $k_y = 0.25\ pNnm^{-1}W^{-1}$ and k_z= $0.09\ pNnm^{-1}W^{-1}$.

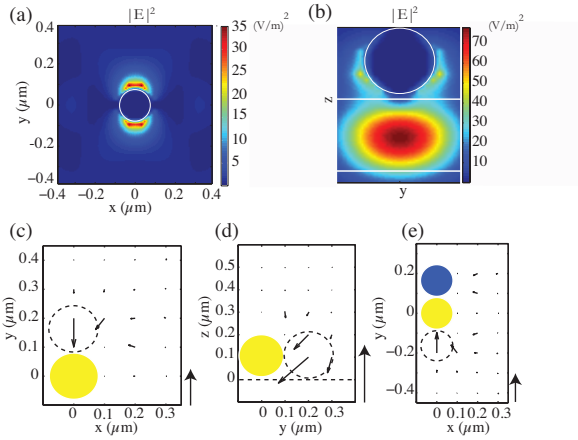

Figure 4.5: Electric field intensity in the midplane (a) and on a vertical cut (b) of a trapped gold particle with r = 80 nm. Horizontal (c) and vertical (d) optical forces as a function of position for a dielectric particle with r = 80 nm in the presence of a trapped gold particle (yellow circle). (e) Horizontal optical force as a function of position for a dielectric particle near trapped gold (yellow) and dielectric (blue) particles. The arrows next to the graph represent Fc / flux = 0.002.

By symmetry, a second possible trapping position exists on the opposite side of the gold particle. Fig. 4.5(e) shows the optical force on a dielectric particle with r = 80 nm after both a gold and dielectric particle are trapped in the locations shown by the solid yellow and blue circles, respectively. The arrow next to the graph represents a value of Fc / flux = 0.002. The dielectric particle is trapped in the position indicated by the dashed line. The results of Fig 4.5 thus indicate that dielectric-metal-dielectric clusters will be formed, consisting of three particles with composition and orientation as shown.

We note that the specific force values and the required power for trapping calculated here assume normally-incident light distributed over an area of approximately 12 μm^2. In an experiment, the coupling efficiency between the incident light and the cavity can likely be increased by adjusting the spot size of the normally-incident beam and/or using a side-coupled waveguide to inject light into the microcavity mode, increasing

the optical forces and reducing the power required for trapping.

In an experiment, surface treatment of the gold nanoparticles, dielectric nanoparticles, and photonic crystal may be required to prevent aggregation, adhesion, and/or electrostatic effects. Previous experimental work in the literature has developed techniques for preventing aggregation of gold (55) and dielectric (61) nanoparticles, as well as adhesion between nanoparticles and microphotonic devices (51). Electrostatic interactions in the system can be minimized using a phosphate buffer solution with a regulated pH of 7.0 (47).

We estimate that the rms variation of the gold particle due to Brownian motion is approximately 20nm for the trap stiffness and power given in the paper. We have calculated the field profile for displacements of the gold particle on this order. We observe that the variation in field intensity is less than 10%. While the symmetry of the intensity distribution is broken slightly due to particle motion, both the qualitative shape and magnitude is largely preserved. We therefore do not expect Brownian motion to significantly affect the conditions for optical trapping.

We have also checked that the force exerted on the gold particle by the dielectric particle is much smaller than the force exerted on the gold particle by the cavity. The Figure below shows the optical forces on the gold (yellow) and dielectric (blue) particles in the configuration at which the forces are strongest. The arrow next to the graph indicates Fc/flux=0.002. We calculate that the force on the gold particle will displace the particle by less than 12nm from the center of the photonic-crystal microcavity. As seen in our answer to point 4 above, displacements on this order will

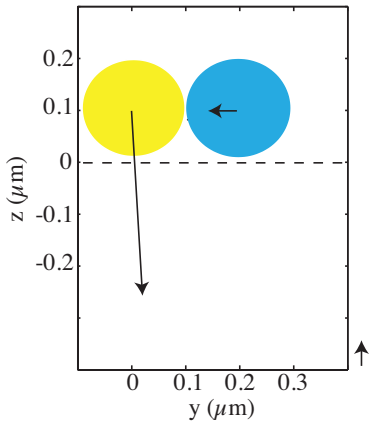

Figure 4.6: Force on gold particle due to dielectric particle.

not significantly change the field profile.

We finally, simulated the heating-induced fluid convection in COMSOL and used Stokes law to estimate the drag force exerted on particles by flow in a 10 μm thick channel. The heating source in the simulation is calculated using the spatially-dependent electric fields obtained from FDTD simulations. For an incident power of 10 mW, the maximum temperature rise is $\sim$ 7 K, and the maximum flow speed is $\sim$ 0.1 nm/s. The normalized drag force ($F_d c$ / flux) on a 80 nm radius gold particle is estimated to be less than 4×10^{-9}, which is negligible compared to the optical trapping force.

In summary, we have proposed a method for using optical forces to induce the formation of metallo-dielectric clusters with controlled morphology. The method relies on field-enhancement effects near gold particles trapped above a photonic-crystal microcavity. If the self-assembly process is performed in a photopolymerizable solution, a secondary laser spot could be used to locally solidify the region around the cluster.

Moreover, integration with a microfluidic channel could allow for controlled, sequential delivery of individual gold and metal particles, along with controlled collection of metallo-dielectric clusters.

Chapter 5

GUV's Bending modulus measurement using Dual-beam optical trap

Dual beam optical trap (DBOT) has seen a growing interest in the field of optical manipulation of biological cells due to its ease of implementation and non-invasive nature. Cells (70) and giant unilamillar vesicles (GUVs)(71), have been successfully trapped and stretched in a DBOT platform, which provide an excellent tool to investigate the membrane elastic properties. Thus, the DBOT provides a method for non-invasive application of time-dependent forces in a device suitable to rapid, high-throughput measurements.

GUVs typically contain the same solution on the interior and exterior of the spherical, lipid bilayer, thus the refractive index difference required for trapping is not present. Here, we used GUVs with different, osmotically-balanced solutions on the interior and exterior of the bilayer. We construct a DBOT based on optical fibers integrated with a capillary flow channel and demonstrate trapping and stretching of a GUV. We characterize the response of the GUV to a step increase in stress. We further conduct experiments in which the area strain of the GUV is measured as a function of applied stress and develop a method to extract the bending modulus of the membrane from the data. This method incorporates three-dimensional ray-tracing methods to calculate the applied stress in the DBOT. The value we obtain for the bending modulus agrees well with literature values. Unlike previous results in the literature (62; 63), we use a laser-wavelength

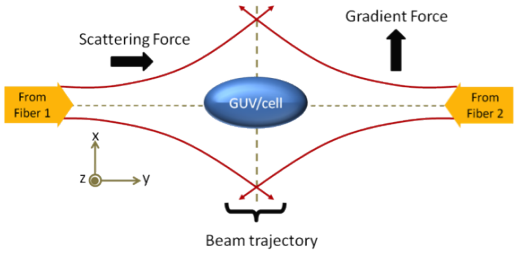

Figure 5.1: Dual-beam optical trap

selected to minimize heating effects (64; 65) avoid the use of polyethylene glycol, which is known to destabilize membranes (66), and model the mechanical properties of the GUV as a lipid bilayer according to the accepted approach developed by Helfrich (67). Our results demonstrate the potential of the DBOT for rapid, flow-through measurements of membrane response to changing physiochemical environments, opening a path for a wide range of biological experiments.

5.1 Stress profile

Counter-propagating beams emitted from two optical fibers form an optical trap due to their Gaussian intensity profile and radiation pressure (Fig 5.1)(72). Though the net force acting on the object in this configuration is zero, it experiences a non-zero surface stress (73). This surface stress deforms the surface by an amount depending upon intrinsic elasticity. Thus, elastic objects like cells and GUVs assume the shape of a prolate spheroid (67) when trapped with an eccentricity dependent upon the trapping power and elasticity. In order to quantify the shape deformation of GUVs and cells, it is of utmost importance to calculate the surface stress profile on spheroidal objects with a refractive index comparable to the cells and GUVs. An exact calculation of optical stress profile on the surface of spheroidal objects is an absolute requirement to quantify

the resultant shape deformation of the object based on its intrinsic elasticity.

5.1.1 Surface stress using Ray Optics

We consider a spheroidal dielectric object illuminated by a single Gaussian beam. The spheroidal surface is resolved into grid points with corresponding azimuthal angle θ varying from 0 to $\pi/2$ and polar angle ϕ from 0 to 2π. In the case of a closed object, a transmitted beam experiences multiple internal reflections. If we consider m internal reflections, the total optical surface stress is (29)

$$\vec{\sigma}_m = \frac{2P_T n_1 T_0 \Delta s cos\theta}{\pi w^2 c \Delta s_m} exp\left(-\frac{2r^2}{w^2}\right) \prod_{j=1}^{m-1} R_j \left[\frac{n_2}{n_1}\hat{i}_m - (\frac{n_2}{n_1}R_m\hat{r}_m + T_m\hat{t}_m)\right] \quad (5.1)$$

The incident vector takes in to account the divergence of the beam, meanwhile the subsequent reflected and transmitted vectors can be computed using Snell's law. The stress due to the first reflection from the incident beam is computed and subsequent surface stress arising from multiple reflection of the transmitted beam are also recorded. Given the symmetries of the system and provided non-polarized light, only the stress calculations in the equatorial plain are needed, any other cut of the spheroid would be a rotation of the equatorial plane.

Fig 5.2, shows the optical stress from the incident beam (σ_1) and the first four internal reflection $(\sigma_2 - \sigma_5)$ for a sheroid of volume equal to 523.6 μm^3 and e = 0.4. The angular range $[0 - \pi/2]$ corresponds to the illuminated part of the object while $[\pi/2 - \pi]$ is the shadowed region. For σ_1 there is a maximum stress in the shadowed region since a larger change in momentum is observed when a ray goes from a higher to lower refractive index. Next, the surface stress from each bounce is added vectorialy

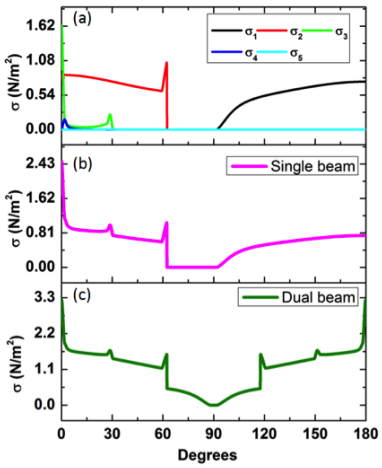

Figure 5.2: (a) Optical stress for multiple reflections on a spheroid with volume equal to a 5 μm sphere and e = 0.4 (n_1 = 1.335, n_2 = 1.38, w = 11 μm). RI of Red Blood Cells is close to the value chosen in this case. (b) Total optical surface stress in the equatorial plane for single beam, and (c) total optical surface stress for dual beam.

to obtain the total optical surface stress profile in the equatorial plane from a single beam (Fig 5.2(b)). As we can see, each reflection introduces a spike in the total surface stress near the region of illumination. These spikes can be understood as an interference phenomenon inside the spheroid for each single beam.

In an experiment, a low coherence source is useful for dual beam optical trapping since it eliminates interference effects. The two trapping beams are incoherent with respect to each other, since the path length difference between the two fibers are much longer than the coherence length of the light. Thus, the stress contribution from the dual beam trap is obtained via vectorial addition of the stress due to the two opposing Gaussian beams (Fig 5.2(c))). As expected, the optical stress is symmetric and the spikes represent interferences from each beam, but not between the beams. In order to corroborate this result we performed the same calculation using the Maxwell Stress tensor method.

5.1.2 Surface stress using the Maxwell Stress tensor

The Maxwell Stress tensor method (MST) express the optical force acting on an object via the change in electromagnetic momentum across the surface of a close object. If we want to consider the optical stress in the surface, we can consider two surfaces, one just above the object interface and one just bellow (28). The total force is then

$$F_{sur} = \oint_{S_{out}} T_{out} \cdot \hat{n} da - \oint_{S_{in}} T_{in} \cdot \hat{n} da \tag{5.2}$$

Expanding the stress tensor matrix in terms of the associated electric and magnetic field components and applying continuity of fields across the surface, the time average surface stress takes the following form

$$\langle \sigma_{sur} \rangle = \frac{\epsilon_0}{4}(n_2^2 - n_1^2) \left[\frac{|D_n|^2}{n_2^2 n_1^2 \epsilon_0^2} + |E_t|^2 \right] \hat{n} \tag{5.3}$$

D_n and E_t are the normal component of electric flux density and tangential component of the electric field respectively and ϵ_0 is the permittivity of vacuum. In agreement with the RO model, the surface stress at any point P is directed along the surface normal $\hat{n}$.

In our simulations, we performed a complete full wave solution of the Maxwell's equations using FDTD analysis to compute the electric fields. We simulated a circularly polarized light to emulate time-averaged unpolarized light. We first simulated the single beam case and computed the corresponding stress components. Using mirror symmetry we flipped the electric field to simulate a counter propagating beam and calculated the stress components. A scalar addition of these two stress components (since both are directed along the surface normal) yields the total contribution from two incoherent

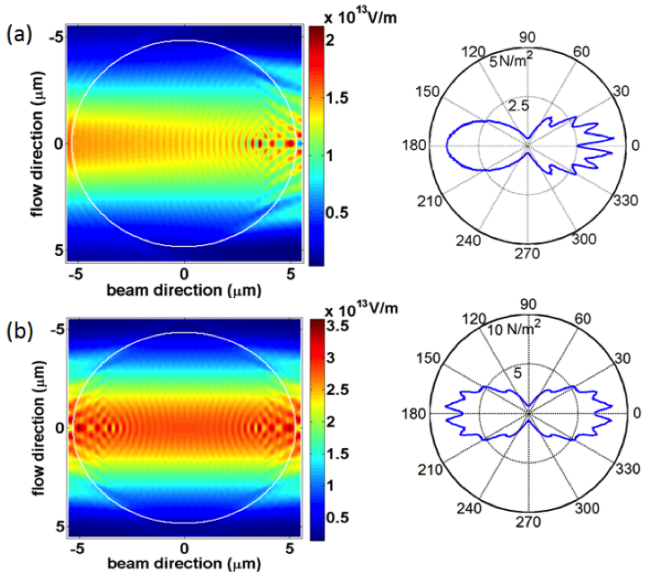

Figure 5.3: Circularly polarized electric field intensity and corresponding stress profile in the equatorial plane for (a) Single Beam (b) Dual beam.

counter propagating beams.

Fig 5.3(a) shows the stress profile and the corresponding field intensity profile on the equatorial plane of a spheroid object with refractive index $n_2 = 1.38$ arising from a single Gaussian beam propagating in a medium with refractive index $n_1 = 1.335$ (initial beam waist $w_0 = 2.4\mu$m and propagation distance of 110μm). The dual beam stress profile and the electric field intensity, obtained by incoherent sum of electric field intensity arising from each beam (Fig 5.3(b)).

5.1.3 Comparison between RO and MST

We carried out a comparison in order to verify the stress profile obtained using RO and MST. We varied the eccentricity, size of the spheroidal object and refractive index contrast between the surrounding medium and the object. In each of the following cases, wavelength is set at 808 nm and the initial beam waist is w_0 = 2.4 μm and the

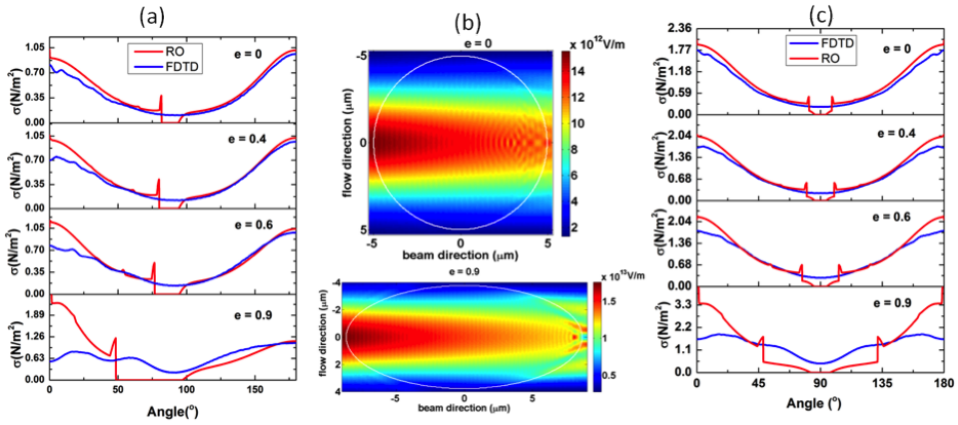

Figure 5.4: Comparison of stress profile arising from single beam in the equatorial plane obtained from ray optics and MST for varying eccentricities (b) single beam electric field intensity profile corresponding to $e = 0.0$ and $e = 0.9$ (c) Dual beam.

medium is assumed to be water which possesses a refractive index n = 1.335. The choice of beam waist and wavelength agree with our experimental set up . In case of refractive index and eccentricity variation the trap center is at distance of 110μm from the beam waist, which makes the ratio of the beam waist, at the trap site, and radius of an equal volume sphere close to 1. In this way, we establish similar illumination conditions for all the cases studied. In first two cases, the volume of the object is kept equal to that of a sphere of radius 5 μm. In case of the size variation, the beam width at the trap center is adjusted by varying the location of the trap site to give a ratio of beam waist to object radius equal to 1.

Fig 5.4 shows a comparison between RO and MST with spheroids of different eccentricities and a refractive index contrast of 0.0105 (similar to what exits in case of GUVs with sucrose and glucose solution inside and outside). Similar to observation made by (28) for spheres, in the single beam case, we also notice that RO and MST analysis matches exactly in the illuminated surface ($\theta = \pi/2$ to π) for spheroids with low eccentricity due to the lack of interference fringes. But in the shadowed

region ($\theta = \pi$ to 2π) the presence of surface waves (74) and fold caustics (75) (region on the shadowed surface where rays from two different angle of incidence strikes) causes wave interference, resulting in the deviation of RO from MST. The first peak in the RO stress profile arises from the first order fold caustics (i.e. on the first reflection from the shadowed region) and as is evident from the figure it broadens with eccentricity due to an enhanced focusing effect. For higher eccentric objects the first order fold caustics exits over a larger region, therefore the interference is more prominent (extreme eccentric case $e = 0.9$). Fig 5.4(b) illustrates the single beam field profile for a sphere ($e = 0$) and highly eccentric prolate spheroid ($e = 0.9$) purporting the fact of enhanced focusing and interference effects. The dual beam case (Fig 5.4(c)) is just an extension of the single beam stress profile and as expected the interference effects now become predominant throughout the surface of the spheroid.

The correlation between RO and MST analysis with refractive index variation and size variation is shown in Fig 5.5. The values of refractive index contrast chosen here agree with those which exist for GUVs ($\Delta n = 0.0105$), RBCs ($\Delta n = 0.045$) and polystyrene ($\Delta n = 0.245$). As refractive index contrast is increased, the angle of refraction increases and rays undergo larger deviation from the incidence direction; consequently the two ray inference zone (first order fold caustics) broadens. This is evident in Fig 5.5(a) where the first peak in the RO analysis becomes wider as we increase the refractive index contrast. This trend leads to enhanced interference effects in the shadowed region and thus causing RO to further deviate from FDTD analysis. However, in case of size variation, the interference effects increase marginally with size and thus the variation between RO from MST remains constant.

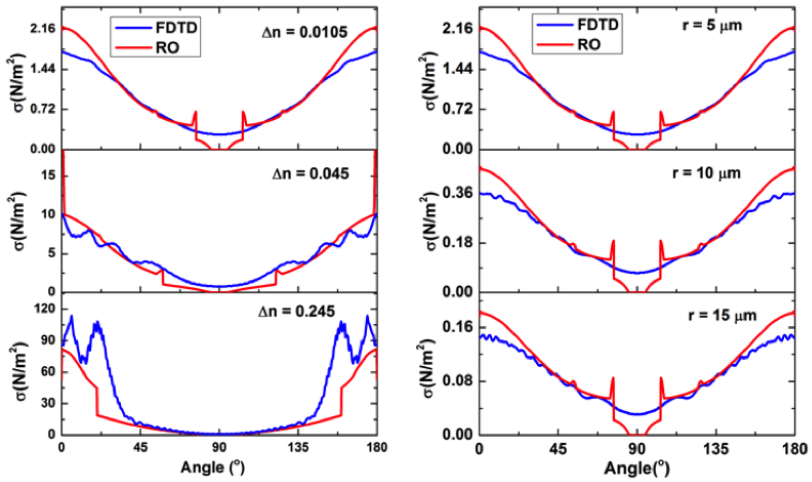

Figure 5.5: Comparison of MST and RO for spheroids with e = 0.4 (a) refractive index variation and (b) size variation.

However, in all the cases studied, it is quite apparent that the area under the stress curves for both the RO and MST remains approximately equivalent. Therefore it is justified in using the RO approximation while calculating the total force on the object. However, for the stress profile calculation, the interference effects on the spheroid surface causes the RO and MST to deviate from one another substantially. Resultantly, for cases where the point of interest is surface stress (as in the case for living cells and GUVs trapped in DBOT) MST provides a more accurate result even if the spheroid size is within the RO limit.

5.2 Dual-beam optical trap setup

A schematic of a dual-beam optical trap is shown in Fig 5.6. Light is emitted from two optical fibers (OF) creating a counter-propagating Gaussian beam trap. The optical fiber used is HI780 (Corning, USA) with $\sim 2.4\mu$m mode-field radius. The beam size at the center of the flow channel ($w_0 = 11.5\mu$m) was calculated from the size of the optical fiber mode using the ABCD matrix method. Radiation pressure pulls the GUV

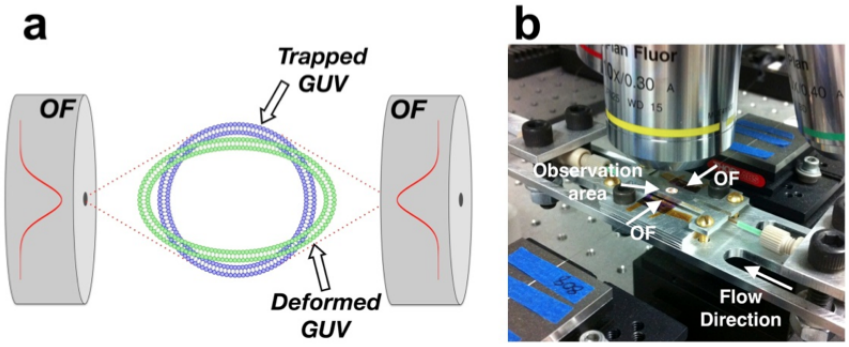

Figure 5.6: (a) Schematic of the stretching of a GUV using DBOT, (b) Optical setup that incorporates a silicon chip for fiber-to-capillary alignment and microfluidic adapters to couple the flow channel.

into the center of the two beams, creating a stable trap (68; 69). In this position, the surface stress (70; 72) can deform the GUV along the beam axis, as shown.

The micro-fluidics channel was created with a square capillary of 100 μm inner diameter (Vitrocom, USA) and a 100 μm wall thickness. The optical fibers were aligned perpendicularly to the micro-fluidics channel at a distance of 300 μm. The axis of each optical fiber was aligned so that the trapping region was at the center of the flow channel; thus trapped GUVs were not in physical contact with capillary walls. The capillary-to-fiber union was coated with index matching liquid, and the capillary is coupled to a peristaltic pump (Instech, USA) using microfluidic adapters (Upchurch, USA).

A wavelength of 808 nm was used and a power output of 250 mW was measured at each fiber. The wavelength was selected to minimize water absorption (76) in the infrared and thereby avoid heating effects (64; 65). For a wavelength of 808 nm, we have simulated the heating of our flow channel in COMSOL and found that the

temperature increases less than 1 K for 250 mW of laser power.

A microscope was used to observe the experiment and a video was recorded at 61 fps by a GiGe camera with CCD image sensor (Basler AG, Germany). Both the laser and camera were controlled through a customized Labview program (National Instruments).

5.3 GUV fabrication

To facilitate trapping, it is necessary to create a refractive index difference between the interior and exterior of the GUV. To achieve this, we fabricated GUVs with an internal sucrose solution and transferred them to an osmotically-balanced glucose solution. The density difference between sucrose and glucose results in a refractive index difference.

GUVs with sucrose inside were fabricated by electroformation from pure dioleoylphosphatidylcholine (DOPC) using a modified vertion of (77). The synthetic lipid, 1-palmitoyl-2-oleoyl-sn-glycero-3-phosphocholine (POPC), 1,2-dipalmitoyl-sn-glycero-3-phosphocholine (DPPC), and cholesterol were purchased from Avanti Polar Lipids (Alabaster, AL). The lipids were dissolved in chloroform and deposited onto an indium-tin oxide (ITO) coated glass slide from Delta Technologies (Loveland, CO). The electroformation chamber was formed with two ITO slides, with the conducting sides facing inwards and separated by a 2.5 mm thick silicone spacer. A 500 mM sucrose solution in 4 mM HEPES titrated to pH 7.0 with sodium hydroxide was added to the overnight vacuum-dried lipid film on the slides giving a final lipid concentration of 0.25 mg/mL. A 2.65 V AC electric field, generated at 100 Hz by a function generator, was applied to the chamber. The electroformation temperatures were chosen so that the lipids remain in the liquid phase. Transfer to a glucose solution was achieved by

performing three two-fold serial dilutions on the GUV suspension using an identical buffer solution, but with the sucrose swapped for an equimolar quantity of glucose.

Refractive indices were measured for the pure sucrose and glucose solutions using a refractometer (PAL-RI Refractometer - Atago, Bellevue, WA). Values were obtained for the pure glucose solution (RI = 1.3455 $\pm$ 0.0003) and sucrose solution (GUV interior RI = 1.3575 $\pm$ 0.0003), and the dilution used in the experiment yielded a final refractive index difference of 0.0105 $\pm$ 0.0003, slightly less than the difference between the two pure solutions. The prepared mixture was then left to sit for ten minutes in order to allow GUVs to sediment to the bottom of the tube. Following this time, half of the total liquid volume was carefully removed at the surface. This suspension was then directly pumped into our microfluidic device.

5.4 Trapping and stretching of GUVs

GUVs were captured using minimal power (total power of 100 mW; 50 mW from each fiber) while ensuring the flow was stopped and the GUV was resting at the bottom of the channel. As a GUV is pulled up toward the optical axis, its initial circular shape is drawn into a slightly prolate elliptical shape due to the stress profile created by the optical stress. Axial deformation of a GUV made of POPC lipid is shown in Fig 5.7(a). The total power was then increased to 500 mW, and the deformed shape at maximum power is shown in Fig 5.7(b). The major axis is increased from $d = 11.53 \pm 0.05$ μm to $d = 11.94 \pm 0.05$ μm along the beam axis, while the minor axis decreased from 10.29 $\pm$ 0.05 μm to 10.05 $\pm$ 0.05 μm. Fig 5.7(c) shows the contours at both minimum and maximum power. Stretching of the GUV along the beam axis can be clearly observed.

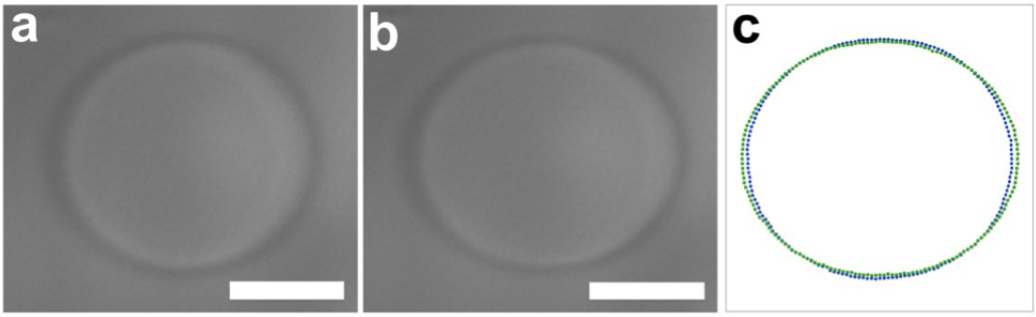

Figure 5.7: (a) POPC-GUV optically trap at low power, (b) POPC-GUV optically trap at high power, (c) A plot of the contours fitted to both stretching powers (blue = low power / low tension, green = high power / high tension). The scale bar is 10 μm.

5.4.1 Calibration of optical forces

The optical power calibration of our DBOT setup was done using shooting experiments. We first trapped a polystyrene bead ($n = 1.615$) in water with equal power from both beams and pushed it towards the one beam by increasing the power of the opposite beam. We then blocked on the opposite beam by reducing the current supplied to zero. The polystyrene bead accelerated towards the opposite beam and the distance vs. time information were recorded. The velocity as a function of distance was then calculated and used in drag force equation, $F_{drag} = 6\pi\eta\rho v$, where η is the viscosity of the water (0.0009 Pa·s), ρ is the radius of polystyrene bead (4.97 μm) and v is the velocity of the particle. The following correction factor was multiplied to the drag force,

$$c = \frac{1}{1 - \frac{9}{16}\left(\frac{\rho}{b}\right) + \frac{1}{8}\left(\frac{\rho}{b}\right)^3 - \frac{45}{256}\left(\frac{\rho}{b}\right)^4 - \frac{1}{16}\left(\frac{\rho}{b}\right)^5} \cdot \frac{2\nu + b\beta}{3\nu + b\beta} \tag{5.4}$$

where b is the distance to the closest wall and β^{-1} is the slip coefficient.

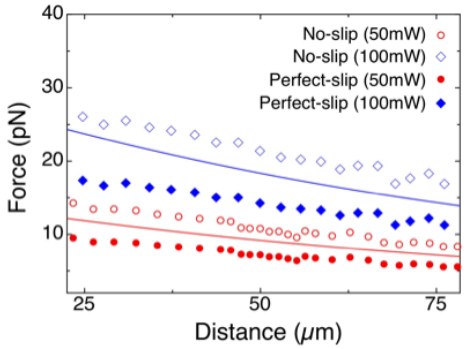

Figure 5.8: The drag forces in no-slip and perfect-slip cases are plotted against the calculated optical forces (solid lines) from one beam for two power levels, 50mW and 100mW. 50 μm corresponds to the center of the channel.

The first term is associated with the proximity of the walls while the second term takes into account the slip-flow boundary conditions on the surface of the particle [36]. The experiment was repeated with two different optical power levels, 50 mW and 100 mW. The corrected drag forces, assuming no-slip conditions ($\beta \rightarrow \infty$), are the upper boundary of the force exerted on the bead. In the case of perfect slip ($\beta \rightarrow 0$), the corrected drag force is the minimum force expected on the bead and therefore our lower boundary. In Fig 5.8 these boundaries were plotted against the theoretical optical forces. Our theoretical prediction of optical force is consistent within these boundaries while the upper boundary matches the theoretical optical force within $\sim$15$\%$ at the center of the channel.

5.4.2 Temporal response to applied stress

We measured the response of a GUV to a step increase in applied stress. The total laser power was increased from 100 mW to 500 mW, as shown in Fig 5.9(a) (blue line; right axis).

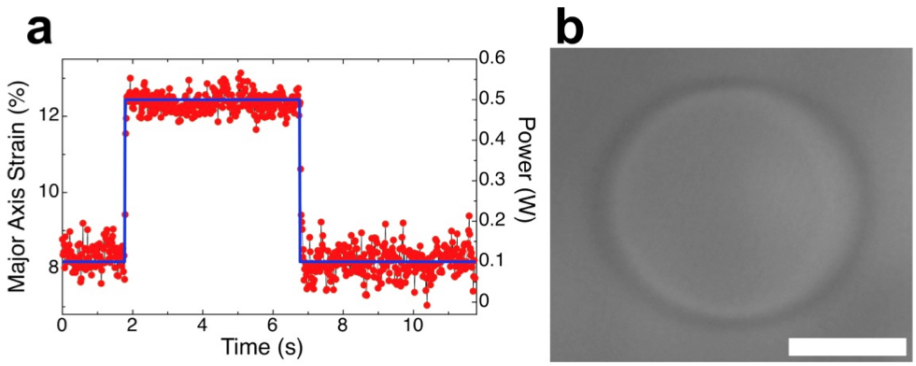

Figure 5.9: (a) The optical power (blue line; right axis) is suddenly increased from 100 mW to 500 mW. The major axis strain is shown by the red dots (left axis). (b) Micrograph of deforming GUV. The scale bar is 10 μm.

The power was held at its maximum value for 5 seconds and then decreased to its initial value. The major axis strain is shown on the left axis (red dots). The major axis strain was calculated by assuming that the shape of the GUV at maximum power is a prolate spheroid. We take the diameter of a sphere with the same volume as the zero-power value of the major axis. The major axis strain is the percent change in major axis compared to the zero-power value. From Fig 5.9(a), it can be seen that the major axis strain increases nearly instantaneously with the step increase in power. The initial strain of $8.2 \pm 0.4\%$ increases by $4.1 \pm 0.25\%$. Based on our frame rate of 61 fps, we are able to capture 2-3 data points in the transition region between power levels.

5.5 Measurement of lipid bilayer bending modulus

In our experiment, we gradually ramped the laser power from 100 mW to 500 mW as shown in Fig 5.10(a). The power was increased in 11 steps, with a holding time of 1 s at each step. As the power increased, we observed axial deformation of the GUV and a clear dampening of membrane fluctuations.

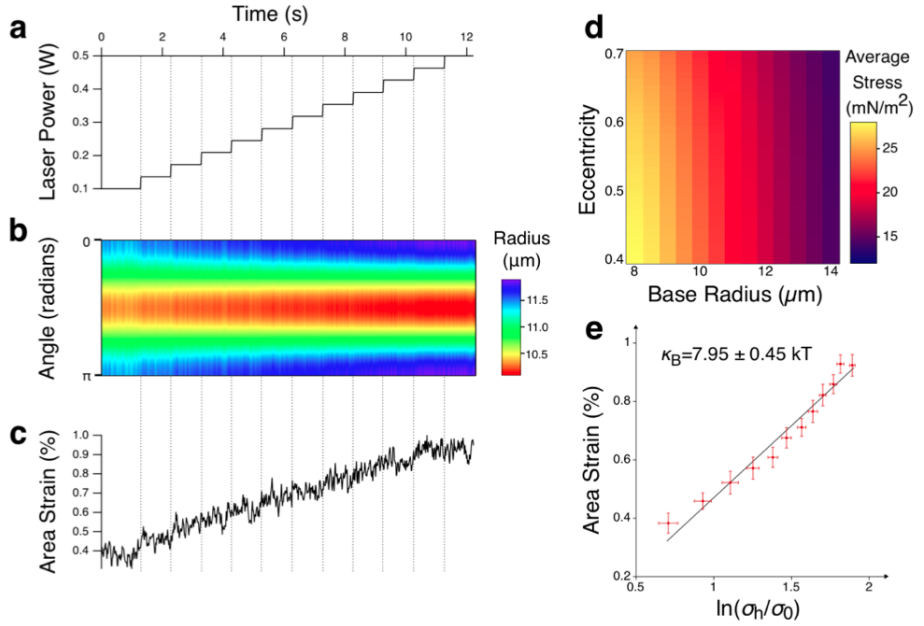

Figure 5.10: Measurement of the bending modulus of a pure POPC GUV. Time axis is common to plots a-c, dotted guide lines show time points at which laser power is increased. (a) Laser power as a function of time. (b) 2D contour plot showing the radius as a function of angle in the image plane as a function of time. (c) Percentage area strain as a function of time. (d) Average stress on the GUV as a function of eccentricity and base radius. (e) Average percentage area strain for each laser power plotted versus the scaled lateral tension. κ is the fitted value of the bending modulus.

We calculate the area strain of a GUV as follows. The grayscale image for each frame was processed using our in-house Matlab code to trace the edge of the GUV. The nominal edge is located at the grayscale center-of-mass in an 8-pixel region surrounding the darkest pixel at each point along the GUV circumference. The edge coordinates formed a closed contour for each frame. The nominal GUV center was located at the center of this contour.

The resulting contour data set for each image frame consists of the location of the contour center and a contour radius for each of 360 azimuthal angular points. Contour

radius can be expressed as a function of azimuthal angle (Fig 5.10(b)). We then proceeded to expand the contour data in Legendre polynomials. This strategy fits the shape of the contour as an expansion of the equatorial plane of a base sphere with radius R. This base sphere is the assumed relaxed shape of the untrapped GUV. To find R, the GUV at minimum trapping power is assumed to be a prolate sphereoid. The volume of this GUV is calculated as $V_0 = 4/3\pi a^2 b$, where a is the semi-minor axis and b is the semi-major axis. R is then the radius of a sphere with the same volume as this prolate spheroid. Initial area is calculated as the surface area of this sphere, $A_0 = 4\pi R^2$. We restrict our Legendre expansion to the second mode coefficient (u_2), since this can be used to represent the shape change of the contour from circle to increasingly eccentric ellipse (78; 79). We reconstructed the contour using the equation,

$$r(\theta) = R + u_2 P_2(cos\theta) \tag{5.5}$$

where

$$P_2(cos\theta) = \frac{1}{2}(3cos^2\theta - 1) \tag{5.6}$$

and u_2, using the ortho-normality of the Legendre polynomials, is given by the integral:

$$u_2 = \frac{5}{2}\int P_2(cos\theta)[r(cos\theta) - R]d\theta \tag{5.7}$$

After reconstruction the contour, the top half the contour [0-π] was numerically integrated to generate a solid of rotation about its major axis corresponding to the surface area of the GUV

$$A = 2\pi \int_0^\pi r sin\theta \sqrt{r^2 + \frac{(dr)^2}{(d\theta)^2}} d\theta \tag{5.8}$$

Area strain is calculated using $(A - A_0)/A_0$ (Fig 5.10(c)). As expected, we observe an increase in area strain with increasing laser power.

The bending modulus κ_B of the GUV membrane can be obtained by calculating area strain as a function of lateral tension. In the low-stress regime (80)

$$\frac{A - A_0}{A_0} = \frac{kT}{8\pi\kappa_B} ln\left(\frac{\sigma_h}{\sigma_0}\right) \tag{5.9}$$

where k is Boltzmanns constant, T is temperature, σ_h is the lateral tension on the membrane, and σ_0 is the intrinsic lateral tension.

In order to determine the lateral tension on the membrane at each power level (81), it is necessary to calculate the surface stress on the GUV. Ray optics approaches have previously been used to calculate the force on spherical (82) and spheroidal (83) objects. We assume a spheroidal shape for the GUV, and calculate the total force on the front and back surfaces. For each power level, we calculated the force on a spheroid with major and minor axes equal to the average values over all image frames. We included the effect of multiple reflections, up to 5 bounces. For each incident ray and each bounce, we determine whether the bounce occurs on the front or back surface and store the vector force. For each surface, we then add the force contributions vectorially to determine the total force on the surface. The stress is calculated by dividing the total force by the surface area.

The calculated average stress is shown in Fig 5.10(d). We present the results as a function of eccentricity (e) and base radius (R). The optical power from each beam was taken to be 250 mW and the refractive index difference (Δn) to be 0.0105. While

the average stress decreases slightly with eccentricity, it substantially decreases with increasing base radius (R), in the 8-14 μm range.

The average stress is then translated to a lateral tension σ_h (81; 78). After each increase in optical power, the GUV reaches an equilibrium shape with a homogeneous surface tension in the membrane. The pressure difference created inside (Δp) is equal on the equator and the poles of the ellipsoid. If we assume that there is no applied stress at the poles, given the ray optics approximation, we can use the Young-Laplace equation to write

$$\Delta p = (c_1 + c_2)_{equ}\sigma_h - T_{equ} = (c_1 + c_2)_{pol}\sigma_h \tag{5.10}$$

where c_1 and c_2 are the principal curvature values at both the equator and the poles, and T_{equ} is the magnitude of stress exerted on the surface at the equator. We calculated the curvatures from the extracted contours. The optical stress T_{equ} was calculated using ray optics. As mentioned before, the surface stress is zero at the poles and the symmetrical discontinuities or spikes in the stress profile around the poles are a result of multiple internal reflections. In our calculation, we included the effects of multiple bounces (up to 5) of each incident ray inside the GUV. For the refractive indices of the interior and exterior of the GUV used in our experiment, the reflection is small (R=0.002$\%$).

We calculate an initial tension (σ_0) of 5.76 $\pm$ 0.25 $\times$ 10^{-5} mN/m and plot area strain as a function of the log of scaled lateral tension in Fig 5.10(e). The error bars on both axes are equal to the standard deviation of the corresponding quantity, taken over all images recorded at a fixed laser power. The slope is proportional to the bending modulus, which is found to be 7.95 $\pm$ 0.45 kT. The log-linear relationship indicates that

we are in the low stress regime and that area expansion of the membrane comes from damping bending fluctuations, as opposed to direct stretching (i.e. area dilation) of the membrane, as observed at higher stresses (84).

We note that the experimental data shown in Figs 5.10(a), 5.10(b), 5.10(c), and 5.10(e) is obtained from a single GUV. Moreover, we note that since the stress is not uniform over the GUV surface, a more sophisticated model of vesicle deformation would include the effects of stress non-uniformity on final shape. This is an interesting area for further research.

5.6 POPC, POPC-col and DPPC bending modulus

Under experimental conditions (at room temperature), both pure POPC and POPC with 20 mol$\%$ cholesterol are in the liquid phase whereas DPPC with 20 mol$\%$ cholesterol is in the gel phase (85).

The bending modulus scales with membrane thickness squared multiplied by the area compressibility modulus ($\kappa \sim h^2 K_a$)(86). Gel-phase bilayers are thicker (87), and the bending modulus of a lipid bilayer in the gel phase is consequentially higher, than that of the same membrane in the liquid phase (88; 89).

We first demonstrated that optical stretching is able to measure the difference in bending modulus of lipid membranes with different phase states. Fig 5.11 presents the dependence of relative area strain on applied tension for two GUV compositions: POPC and DPPC with 20 mol$\%$ cholesterol. The initial tensions are at 7.53 $\pm$ 0.73 $\times$ 10^{-5}

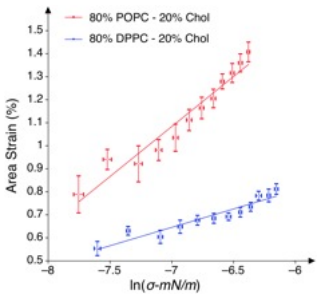

Figure 5.11: Apparent area strain versus ln(tension) plots for POPC and DPPC GUVs with 20% cholesterol. The POPC lipid membrane is more flexible than DPPC lipid membrane. The error bars represent one standard deviation of area strain and lateral tension. The errors in bending modulus values are calculated from the standard errors of the slope using linear regression analysis.

mN/m and $1.61 \pm 0.19 \times 10^{-5}$ mN/m, and the calculated bending modulus values are 9.16 ± 0.72 kT and 24.89 ± 2.47 kT for the POPC and DPPC membrane respectively.

To obtain population statistics, we measured the bending moduli of GUVs fabricated from pure POPC (n = 56), POPC with 20 mol% cholesterol (n = 40), and DPPC with 20 mol% cholesterol (n = 39) respectively. We made fit normal distributions to the data to obtain the following bending modulus means and standard deviations: 8.13 ± 2.06 kT for POPC vesicles, 8.50 ± 1.83 kT for POPC with 20%Chol, and 27.24 ± 7.69 kT for DPPC with 20%Chol. Histograms of the population bending modulus data are given in Fig 5.12.

We confirmed the normality of the populations collected using the Kolmogorov-Smirnov test. We then performed the students t-test to compare the two POPC populations (POPC and POPC-20%Chol). The populations are not significantly different ($p > 0.05$). This analysis confirmed the indistinguishability of POPC populations with and without cholesterol, in contrast to other published results (90; 91). Cholesterol is believed to increase κ by ordering the acyl chains. Marsh did an extensive comparison

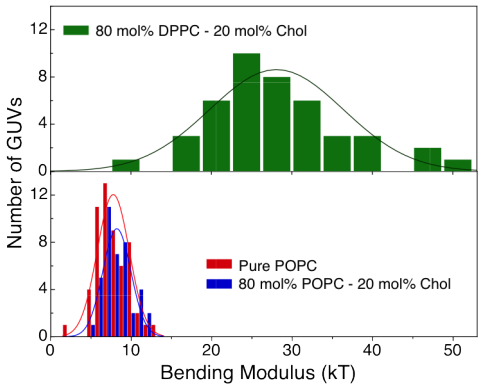

Figure 5.12: Histograms of the bending modulus distributions of and DPPC-Chol, POPC-Chol, and pure POPC lipid GUVs.

of several methods and concluded that cholesterol increases mean bending moduli (92). However recent reports have argued that the contribution of cholesterol to bending modulus is not universal and unsaturated lipids (particularly 1,2-dioleoyl-sn-glycero-3-phosphocoline, DOPC) are not affected by the addition of cholesterol (78; 93). Our results agree with these recent reports. We were unable to produce high yields of pure DPPC GUVs.

There are several factors that may influence the width of the distributions shown in Fig 5.12. GUVs made from POPC may be photooxidized when exposed to bright light during microscopy (94). However, in our optical stretching experiment, the experimental duration for a single GUV was around 30s, and no fluorescent dye was used, so we do not expect significant photooxidation to occur. The width of the DPPC/cholesterol distribution may also be a result of compositional heterogeneity due to non-uniform cholesterol incorporation during lipid film drying, as has been shown previously (95).

We analyzed possible sources of systemic error in this experiment. One potential error source comes from how we calculated vesicle surface area, by fitting the thermal undulations. For the data presented in Fig 5.12, only the second Legendre coefficient is used to calculate the area change. When we include the fourth mode, as suggested in by Gracia and coworkers (78), the bending modulus values tend to decrease by approximately 5%, within the reported error. Including the fourth mode does not decrease the width of the population histograms, indicating that lack of precision in shape fitting is not a major contributor to the width of the observed distributions.

Second, GUVs are trapped at a position slightly below the axis of the optical trap due to gravity. For example, consider a spheroidal GUV with 10 μm equivalent sphere volume and eccentricity of 0.4. The net gravitational force on the GUV is proportional to the density difference between the solutions on the inside and outside and equals $\sim$1.3 pN. The trapping position can be calculated by balancing the gravitational force with the optical gradient force. At the minimum trapping power of 100 mW, the GUV is trapped $\sim$2 μm below the optical axis. At a power of 500 mW, the offset decreases to $\sim$ 0.4 μm. The microscope is initially focused on the equatorial plane of the GUV. As the GUV is pulled further upward into the trap, the segment of the vesicle in the focal plane will shift.

To test whether this effect could have a significant impact on the results, we calculated the volume of the GUV at every frame by assuming the captured contour corresponded to the equatorial plane of a spheroidal vesicle and measuring the length of the major and minor axes. If the upward shift of the GUV were significant, it would be expected to result in consistently smaller measured GUV volumes as power increased. This is because the true volume of the GUV (expected to remain constant through this

experiment) can be calculated from the true equatorial plane contour measured when the microscope is initially focused at minimum trapping power. Contours corresponding to other GUV cross-sections would result in a smaller calculated volume. A significant shift of the vesicle along the optical axis would therefore result in an apparent (and purely artifactual) decrease in volume. In fact, in no experiment did the average calculated volume change exceed 1%, and there was no relationship between volume and power.

Finally, we performed a set of experiments to test whether the GUV stretching system exhibits hysteresis. The optical power was ramped up and down between minimum and maximum trapping power. The bending modulus was obtained both as the vesicle dilated and contracted. Fig 5.13 shows two examples of time-dependent area strain and extracted area strain vs. surface tension, for pure POPC (Fig 5.13(a)) and DPPC-20%Chol (Fig 5.13(b)). For this POPC vesicle, the bending modulus values obtained from the two slopes gave 6.52 $\pm$ 0.32 kT for ramp-up and 6.58 $\pm$ 0.35 kT for ramp-down. For this DPPC-20%Chol vesicle, we obtained 27.47 $\pm$ 3.29 kT for ramp-up and 28.04 $\pm$ 2.25 kT for ramp-up and ramp-down. In all cases tested, the change in measured bending modulus for the two different deformation directions is within error.

In conclusion, we have used optical stretching in a microfluidic DBOT system to investigate the elastic bending modulus of populations of POPC, POPC with 20% Chol, and DPPC with 20% Chol GUVs. The difference in bending modulus between liquid and gel-phase GUVs is unambiguous; gel-phase GUVs are significantly stiffer. The bending elastic modulus of the membrane composed of the monounsaturated phospholipid (POPC) is insensitive to Chol at concentrations up to 20%. This technique is a

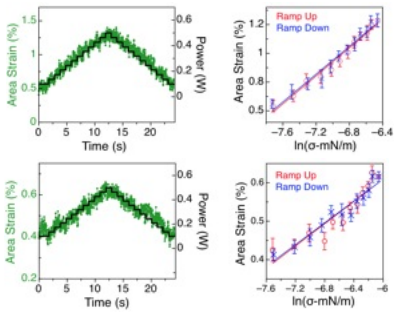

Figure 5.13: Laser power ramp-up and ramp-down experiments on two different GUVs, (a) POPC and (b) DPPC-20%Chol.

simple and powerful approach to the measurement of membrane bending properties. It has the potential to be widely deployed in efforts to understand relationships between membrane composition and membrane mechanics.

Reference List

[1] J. D. Joannopoulos, S. G. Johnson, J. N. Winn, and R. D. Meade, ”Photonic Crystals: Molding the Flow of Light,” 2nd ed. (Princeton University Press, Princeton, 2008).

[2] Whitesides, G.M. and B. Grzybowski, ”Self-assembly at all scales,” Science, 2002. 295: p. 2418-2421.

[3] Yin, Y., et al., ”Template-assisted self-assembly: a practical route to complex aggregates of monodispersed colloids with well-defined sizes, shapes, and structures,” Journal of the American Chemical Society, 2001. 123: p. 8718- 8729.

[4] Van Blaaderen, A., R. Ruel, and P. Wiltzius, ”Tempate-directed colloidal crystallization,” Nature, 1997. 385: p. 321-324.

[5] Ashkin, A., et al., ”Observation of a single- beam gradient force optical trap for dielectric particles,” Opt. Lett., 1986. 11(288).

[6] Ashkin, A., J.M. Dziedzic, and T. Yamane, ”Optical trapping and manipulation of single cells using infrared laser beams,” Nature, 1987. 330: p. 769 - 771.

[7] Okamoto, K. and S. Kawata, ”Radiation force exerted on subwavelength particles near a nanoaperture,” Physical Review Letters, 1999. 83(22): p. 4534-4537.

[8] Wilson, B.K., et al., ”Nanostructure-enhanced laser tweezers for efficient trapping and alignment of particles,” Optics Express, 2010. 18: p. 16005-16013.

[9] Barth, M. and O. Benson, ”Manipulation of dielectric particles using photonic crystal cavities,” Applied Physics Letters, 2006. 89(25): p. 253114.

[10] Rahmani, A. and P.C. Chaumet, ”Optical trapping near a photonic crystal,” Opt. Express, 2006. 14(13): p. 6353-6358.

[11] Yang, A.H.J., et al., ”Optical manipulation of nanoparticles and biomolecules in sub-wavelength slot waveguides,” Nature, 2009. 457: p. 71-75.

[12] Wang, K., E. Schonbrun, and K.B. Crozier, ”Propulsion of Gold Nanoparticles with Surface Plasmon Polaritons: Evidence of Enhanced Optical Force from Near-Field Coupling between Gold Particle and Gold Film,” Nano Letters, 2009. 9(7): p. 2623-2629.

[13] Grigorenko, A.N., et al., ”Nanometric optical tweezers based on nanostructured substrates,” Nature Photonics, 2008. 2: p. 365-370.

[14] Dholakia, K., et al., ”Optical Trapping Takes Shape: The Use of Structured Light Fields, in Advances In Atomic, Molecular, and Optical Physics,” 2008, Academic Press. p. 261-337.

[15] Grier, D.G., ”A revolution in optical manipulation,” Nature Photonics, 2003. 424(6950): p. 810-816.

[16] Reece, P.J., V. Garces-Chavez, and K. Dholakia, ”Near-field optical micromanipulation with cavity enhanced evanescent waves,” Applied Physics Letters, 2006. 88: p. 221116.

[17] Fan, S. and J.D. Joannopoulos, ”Analysis of guided resonances in photonic crystal slabs,” Phys. Rev. B, 2002. 65: p. 235112.

[18] Ladavac, K., Kasza, K., and Grier, D.G. ”Sorting mesoscopic objects with periodic potential landscapes: Optical fractionation,” Physical Review E 70 (2004).

[19] Faucheux, L.P., Bourdieu, L.S., Kaplan, P.D. and Libchaber, A.J. ”Optical thermal ratchet,” Physical Review Letters 74 (1995).

[20] Burns, M.M., Fournier, J.-M., and Golovchenko, J.A. ”Optical matter: Crystallization and binding in intense optical fields,” Science 249 (1990).

[21] Lidorikis, E., Q. Li, and C.M. Soukoulis, ”Optical bistability in colloidal crystals,” Physical Review E, 1997. 55(3): p. 3613-3618.

[22] Antonoyiannakis, M.I. and J.B. Pendry, ”Electromagnetic forces in photonic crystals,” Physical Review B, 1999. 60(4): p. 2363.

[23] Jackson, J. D., ”Classical Electrodynamics,” Third Edition, Hoboken, NJ, 1999: John Wiley and Son.

[24] S. Albaladejo, M. Marques, M. Laroche, and J.Saenz, ”Scattering Forces from the Curl of the Spin Angular Momentum of a Light Field,” Physical Review Letters 102, 113602 (2009).

[25] R. Gomez-Medina, M. Nieto-Vesperinas, and J. Saenz, ”Nonconservative electric and magnetic optical forces on submicron dielectric particles,” Physical Review A 83, 033825 (2011).

[26] P. C. Chaumet and M. Nieto-Vesperinas, ”Time-averaged total force on a dipolar sphere in an electromagnetic field”, Optics Letters, 25, 1065 (2000).

[27] K. Dholakia and P. Zemanek, ” Colloquium: Gripped by light: Optical binding,” Reviews of Modern Physics, 82, 1767 (2010).

[28] Feng Xu, J.A.L., Grard Gouesbet, Cameron Tropea, ” Optical stress on the surface of a particle: Homogeneous sphere,” Physical Review A, 79(5), 053808 (2009).

[29] J. Zhou, M. Zhong, Z. Wang, and Yin-Mei Li,” Calculation of optical forces on an ellipsoid using vectorial ray tracing method,” Optics Express 20, 14928 (2012).

[30] Y. Xia, B. Gates, and Z.-Y. Li, ”Self-assembly approaches to three-dimensional photonic crystals,” Advanced Materials 13, 409-413 (2009).

[31] K. S. Kunz and R. J. Luebbers, ”The Finite-Difference Time-Domain Method for Electromagnetics” (CRC Press, Boca Raton, 1993).

[32] A. F. Oskooi, D. Roundy, M. Ibanescu, P. Bermel, J. D. Joannopoulos, and S. G. Johnson, ”MEEP: A flexible free-software package for electromagnetic simulations by the FDTD method,” Computer Physics Communications 181, 687-702 (2010).

[33] J. Pan, Y. Huo, K. Yamanaka, S. Sandhu, L. Scaccabarozzi, R. Timp, M. L. Povinelli, S. Fan, M. M. Fejer, and J. S. Harris, ”Aligning microcavity resonances in silicon photonic-crystal slabs using laser-pumped thermal tuning,” Appl. Phys. Lett. 92, 103114 (2008).

[34] J. H. Lee, Q. Wu, and W. Park, ”Metal nanocluster metamaterial fabricated by the colloidal self-assembly,” Opt. Lett. 34, 443-445 (2009).

[35] Mejia, C.A., Dutt, A. and Povinelli, M.L. ”Light-assisted templated self-assembly using photonic crystal slabs,” Optics Express 19, 11422-11428 (2011).

[36] Ma, J., Martnez, L.J. and Povinelli, M.L. ”Optical trapping via guided resonance modes in a slot-Suzuki-phase photonic crystal lattice,” Optics Express 20, 6816-6824 (2012).

[37] Neuman, K.C., and Block, S.M. ”Optical trapping,” Review of Scientific Instruments 75 (2004).

[38] Erickson, D., Serey, X., Chen, Y.-F. and Mandal, S. ”Nanomanipulation using near field photonics,” Lab on a Chip 11, 995-1009 (2011).

[39] Crocker, J.C., and Grier, D.G. ”Methods of digital video microscopy for colloidal studies,” Journal of Colloid and Interface Science 179, 298-310 (1996).

[40] Wong, W.P., and Halvorsen, K. ”The effect of integration time on fluctuation measurements: calibrating an optical trap in the presence of motion blur,” Optics Express 14, 12517-12531 (2006).

[41] M. Gullans, T. G. Tiecke, D. E. Chang, J. Feist1, J. D. Thompson, J. I. Cirac, P. Zoller, and M. D. Lukin, ”Nanoplasmonic Lattices for Ultracold Atoms,” Physical review letters 109, 235309 (2012).

[42] C. Dineen, M. Reichelt, S. W. Koch and J. V. Moloney, ”Optical trapping of quantum dots in a metallic nanotrap,” J. Opt. A: Pure Appl. Opt. 11, 114004 (2009).

[43] X. Serey, S. Mandal, YF. Chen, D. Erickson, ”DNA transport and delivery in thermal gradients near optofluidic resonators,” Physical review letters, 108, 048102 (2012).

[44] T. Iida , H. Ishihara, ”Theoretical study of the optical manipulation of semiconductor nanoparticles under an excitonic resonance condition,” Physical review letters, 90, 057403 (2003).

[45] L. Huang and O. Martin, ”Reversal of the optical force in a plamonic trap,” Optics Letters 33, 3001 (2008).

[46] T. Li, S. Kheifets, and M. Raizen,”Millikelvin cooling of an optically trapped microsphere in vacuum,” Nature Physics 7, 527 (2011).

[47] B. S. Schmidt, A. H. Yang, D. Erickson, and M. Lipson, ”Optofluidic trapping and transport on solid core waveguides within a microfluidic device,” Optics Express, 22, 14322 (2007).

[48] A. Einat, U. Levy, ”Analysis of the optical force in the Micro Ring Resonator,” Opt Express 19, 20405 (2011).

[49] B. Roxworthy, K. Ko, A. Kumar, K. Fung, E. Chow, G. Liu, N. X. Fang, and K. C. Toussaint ”Application of Plasmonic Bowtie Nanoantenna Arrays for Optical Trapping, Stacking, and Sorting,” Nano Letters, 12, 796 (2012).

[50] Y. Tanaka and K. Sasaki, ”Efficient optical trapping using small arrays of plasmonic nanoblock pairs,” Appl. Phys. Lett. 100, 021102 (2012).

[51] S. Mandal, X. Serey, and D. Erickson, ”Nanomanipulation Using Silicon Photonic Crystal Resonators”, Nano Letters 10, 99 (2010).

[52] C. Renaut, J. Dellinger, B. Cluzel, T. Honegger, D. Peyrade, E. Picard, F. de Fornel, and E. Hadji, ”Assembly of microparticles by optical trapping with a photonic crystal nanocavity,” Appl. Phys. Lett. 100, 101103 (2012).

[53] J. R. Arias-Gonzalez and M. Nieto-Vesperinas, ”optical forces on small particles: attractive and repulsive nature and plasmon-resonance conditions,” J. Opt. Soc. Am. A 20(2003).

[54] F. Hajizadeh and S. N. S.Reihani, ”Optimized optical trapping of gold nanoparticles,” Optics express 18, 551-559 (2010).

[55] L. Bosanac, T. Aabo, P. M. Bendix, and L. B. Oddershede, ”Efficient optical trapping and visualization of silver nanoparticles.,” Nano Letters 8, 1486-1491 (2008).

[56] A. S. Zelenina, R. Quidant, and M. Nieto-Vesperinas, ”Enhanced optical forces between coupled resonant metal nanoparticles,” Opt. Lett. 32, 1156-1158 (2007).

[57] M. Ploschner, M. Mazilu, T. F. Krauss, and K. Dholakia, ”Optical forces near a nanoantenna,” Journal of Nanophotonics 4, 041570-041513 (2010).

[58] L. B. Scaffardi and J. O. Tocho, ”Size dependence of refractive index of gold nanoparticles,” Science 17, 1309-1315 (2006).

[59] K. L. Kelly, E. Coronado, L. L. Zhao, and G. C. Schatz, ”The Optical Properties of Metal Nanoparticles: The Influence of Size, Shape, and Dielectric Environment,” The Journal of Physical Chemistry B 107, 668-677 (2002).

[60] A. H. J. Yang and D. Erickson, ”Stability analysis of optofluidic transport on solid-core waveguiding structures,” Nanotechnology 19, 045704 (2008).

[61] M. L. Juan, R. Gordon, Y. Pang, F. Eftekhari and R. Quidant, Nat. Phys. 5, 915 (2009).

[62] 18. T. M. Pinon, L. S. Hirst, and J. E. Sharping, Fiber-based dual-beam optical trapping system for studying lipid vesicle mechanics, in Optical Trapping Applications, OSA Technical Digest (CD) (Optical Society of America, 2011), paper OTTuB2.

[63] 19. T. M. Pinon, L. S. Hirst, and J. E. Sharping, Optical trapping and stretching of lipid vesicles, in CLEO: Applications and Technology, OSA Technical Digest (online) (Optical Society of America, 2012), paper ATh1M.4.

[64] S. Ebert, K. Travis, B. Lincoln, and J. Guck, Fluorescence ratio thermometry in a microfluidic dual-beam laser trap, Opt. Express 15(23), 1549315499 (2007).

[65] F. Wetzel, S. Rnicke, K. Mller, M. Gyger, D. Rose, M. Zink, and J. KŁs, Single cell viability and impact of heating by laser absorption, Eur. Biophys. J. 40(9), 11091114 (2011).

[66] 22. M. Yamazaki and T. Ito, Deformation and instability in membrane structure of phospholipid vesicles caused by osmophobic association: mechanical stress model for the mechanism of poly(ethylene glycol)-induced membrane fusion, Biochemistry 29(5), 13091314 (1990).

[67] W.Helfrich, "Lipid bilayer spheres - Deformation and birefringence in magnetic-fields," Physical Letters A, 1973. 43: p. 409-410.

[68] A. Ashkin, Acceleration and trapping of particles by radiation pressure, Phys. Rev. 24, 156 (1970).

[69] G. Roosen, A theoretical and experimental study of the stable equilibrium positions of spheres levitated by two horizontal laser beams, Opt. Commun. 21(1), 189194 (1977).

[70] J. Guck, S.S., B. Lincoln, F. Wottawah, S. Ebert, M. Romeyke, D. Lenz, H. M. Erickso, R. Ananthakrishnan, D. Mitchell, J. Kas, S. Ulvick and C. Bilby, "Optical Deformability as an Inherent Cell Marker for Testing Malignant Transformation and Metastatic Competence," Biophysical Journal, 2005. 88: p. 3689-3698.

[71] M. Solmaz, R.B., S. Sankhagowit, J. Thompson, C. Mejia, N. Malmstadt, and M. Povinelli, "Optical Stretching of Giant Unilamellar Vesicles with an Integrated Dual-beam Optical Trap," Biomedical Optics Express, 2012. 3(10): p. 2419-2427

[72] J. Guck, R.A., T. J. Moon, C. C. Cunningham, and J. KŁs, ”Optical Deformability of Soft Biological Dielectrics,” Physical Review Letters, 2000. 84(23): p. 5451-5454.

[73] Paul B. Bareil, Y.S., Arthur Chiou, ”Local stress distribution on the surface of a spherical cell in an optical stretcher,” Optics Express, 2006. 14(25): p. 12503-12509.

[74] Nussenzveig, H.M., ”High-frequency scattering by an impenetrable sphere,” Annals of Physics, 1965. 34(1): p. 23-95.

[75] Upstill, M.V.B.C. Catastrophe ”Optics: Morphologies of caustics and their Diffreaction Pattern,” Progress In Optics. 1980.

[76] L. Kou, D. Labrie, and P. Chylek, Refractive indices of water and ice in the 0.65- to 2.5-?m spectral range, Appl. Opt. 32(19), 35313540 (1993).

[77] M. Angelova, S. Solau, P. Mlard, F. Faucon, and P. Bothorel, Preparation of giant vesicles by external AC electric fields. Kinetics and applications, Prog. Colloid Polym. Sci. 89, 127131 (1992).

[78] R. S. Gracia, N. Bezlyepkina, R. L. Knorr, R. Lipowsky, and R. Dimova, Effect of cholesterol on the rigidity of saturated and unsaturated membranes: fluctuation and electrodeformation analysis of giant vesicles, Soft Matter 6(7), 14721482 (2010).

[79] P. M. Vlahovska, R. S. Graci, S. Aranda-Espinoza, and R. Dimova, Electrohydrodynamic model of vesicle deformation in alternating electric fields, Biophys. J. 96(12), 47894803 (2009).

[80] E. Evans and W. Rawicz, Entropy-driven tension and bending elasticity in condensed-fluid membranes, Phys. Rev. Lett. 64(17), 20942097 (1990).

[81] M. Kummrow and W. Helfrich, Deformation of giant lipid vesicles by electric fields, Phys. Rev. A 44(12), 83568360 (1991).

[82] E. Sidick, S. D. Collins, and A. Knoesen, Trapping forces in a multiple-beam fiber-optic trap, Appl. Opt. 36(25), 64236433 (1997).

[83] H. Sosa-Martinez and J. C. Gutierrez-Vega, Optical forces on a Mie spheroidal particle arbitrarily oriented in a counterpropagating trap, J. Opt. Soc. Am. B 26(11), 21092116 (2009).

[84] J. R. Henriksen and J. H. Ipsen, Measurement of membrane elasticity by micro-pipette aspiration, Eur Phys J E Soft Matter 14(2), 149167 (2004).

[85] Feigenson, G. W.; Buboltz, J. T., "Ternary Phase Diagram of Dipalmitoyl-PC/Dilauroyl-PC/Cholesterol: Nanoscopic Domain Formation Driven by Cholesterol," Biophysical Journal 2001, 80, (6), 2775-2788.

[86] Evans, E. A., "Bending Resistance and Chemically Induced Moments in Membrane Bilayers," Biophysical Journal 1974, 14, (12), 923-931.

[87] Nagle, J. F.; Tristram-Nagle, S., "Structure of lipid bilayers," Biochimica et Biophysica Acta (BBA) - Reviews on Biomembranes 2000, 1469, (3), 159-195.

[88] Mecke, K. R.; Charitat, T.; Graner, F. ., "Fluctuating Lipid Bilayer in an Arbitrary Potential: Theory and Experimental Determination of Bending Rigidity," Langmuir 2003, 19, (6), 2080-2087.

[89] Heimburg, T., "Mechanical aspects of membrane thermodynamics. Estimation of the mechanical properties of lipid membranes close to the chain melting transition from calorimetry," Biochimica et Biophysica Acta (BBA) - Biomembranes 1998, 1415, (1), 147-162.

[90] Henriksen, J.; Rowat, A. C.; Ipsen, J. H., "Vesicle fluctuation analysis of the effects of sterols on membrane bending rigidity," European Biophysics Journal 2004, 33, (8), 732-741.

[91] Arriaga, L. R.; Lopez-Montero, I.; Monroy, F.; Orts-Gil, G.; Farago, B.; Hellweg, T., "Stiffening Effect of Cholesterol on Disordered Lipid Phases: A Combined Neutron Spin Echo + Dynamic Light Scattering Analysis of the Bending Elasticity of Large Unilamellar Vesicles," Biophysical Journal 2009, 96, (9), 3629-3637.

[92] Marsh, D., "Elastic curvature constants of lipid monolayers and bilayers," Chemistry and Physics of Lipids 2006, 144, (2), 146-159.

[93] Pan, J.; Mills, T. T.; Tristram-Nagle, S.; Nagle, J. F., "Cholesterol Perturbs Lipid Bilayers Non-universally," Physical Review Letters 2008, 100, (19), 198103.

[94] Ayuyan, A. G.; Cohen, F. S., "Lipid Peroxides Promote Large Rafts: Effects of Excitation of Probes in Fluorescence Microscopy and Electrochemical Reactions during Vesicle Formation," Biophysical Journal 2006, 91, (6), 2172-2183.

[95] Baykal-Caglar, E.; Hassan-Zadeh, E.; Saremi, B.; Huang, J., "Preparation of giant unilamellar vesicles from damp lipid film for better lipid compositional uniformity," Biochimica et Biophysica Acta (BBA) - Biomembranes 2012, 1818, (11), 2598-2604.